Stony Brook University

Nanoscale metal – organic ligand interactions for applications in environmental remediation and catalysis

A Dissertation Presented

by

Prashant Kumar Jha

to

The Graduate School

in Partial Fulfillment of the

Requirements

for the Degree of

Doctor of Philosophy

in

Materials Science and Engineering

Stony Brook University

December 2011

Stony Brook University

The Graduate School

Prashant Kumar Jha

We, the dissertation committee for the above candidate for the

Doctor of Philosophy degree, hereby recommend

acceptance of this dissertation.

Dr. Gary P. Halada- Dissertation Advisor
Associate Professor-Department of Materials science and engineering

Dr. Dilip Gersappe - Chairperson of Defense
Professor-Department of Materials science and engineering

Dr. Yizhi Meng
Assistant Professor-Department of Materials science and engineering

Dr. Chad Korach
Assistant Professor-Department of Mechanical engineering

This dissertation is accepted by the Graduate School

Lawrence Martin
Dean of the Graduate School

Abstract of the Dissertation

Nanoscale Metal – organic ligand interactions for applications in environmental remediation and catalysis

by

Prashant Kumar Jha

Doctor of Philosophy

in

Materials Science and Engineering

Stony Brook University

2011

Ever since the proposal of correct structure of $CoCl_3 \cdot 6NH_3$ by Alfred Werner in 1893 the field of coordination chemistry has only grown and has become the center of chemical science owing to wide ranging applications in the fields of catalysis, medicine, biochemistry and organometallic chemistry. This dissertation deals with novel application of coordination chemistry from three different perspectives. The first explores the fate of a known contaminant (uranyl ion) in ground water with natural organic matter (NOM) using simple analogous aromatic and aliphatic molecules (catechol and oxalic acid). It was found that not only the immediate complex formed, long term interactions between the metal ion and the organic molecule need to be taken into account for any remediation

process, as uranyl can act as a catalyst in polycondensation of polyphenols. The second part deals with modifying a natural polysaccharide to improve its metal complexation capacity using photochemical enhancement in an electrochemical pathway. Metal adsorption capacity of the novel polymer was tested with oxyanions ($Cr_2O_7^{2-}$) as well as oxycations (UO_2^{2+}). It was found that a model based on monolayer adsorption occurring on an energetically uniform surface without interactive molecules best explained adsorption and kinetics of the reaction followed a pseudo second order model.

In the final part strong complex formation between chitosan and metal ions was exploited to grow stable nanoparticles for catalysis applications. Protonated chitosan was deposited on stainless steel using an electrochemically-induced localized zone of high pH near the electrode. The hydrogel layer was found to be well adhered and conductive. The nature of conductivity is not known but was found to be sufficient for subsequent electro-reduction of silver salt to metallic nanoparticles. Nanoparticle size as well as distribution over the chitosan layer was optimized by controlling operating parameters including voltage, time of deposition and thickness of polymer film. The reduced nanoparticles were tested for their catalytic activity using the oxygen reduction reaction (ORR) and it was found that under oxidative potentials the silver nanoparticles were not just stable up to oxygen reduction potential under alkaline conditions (0.23V Vs Ag/AgCl) but they exceeded the limit by 200mV thus

providing a very broad electrochemical window for the 4 electron pathway for oxygen reduction. The stability of silver is expected to have increased due to complex formation with amine as well as hydroxyl group in chitosan.

Dedicated to

My parents.

Frontispiece

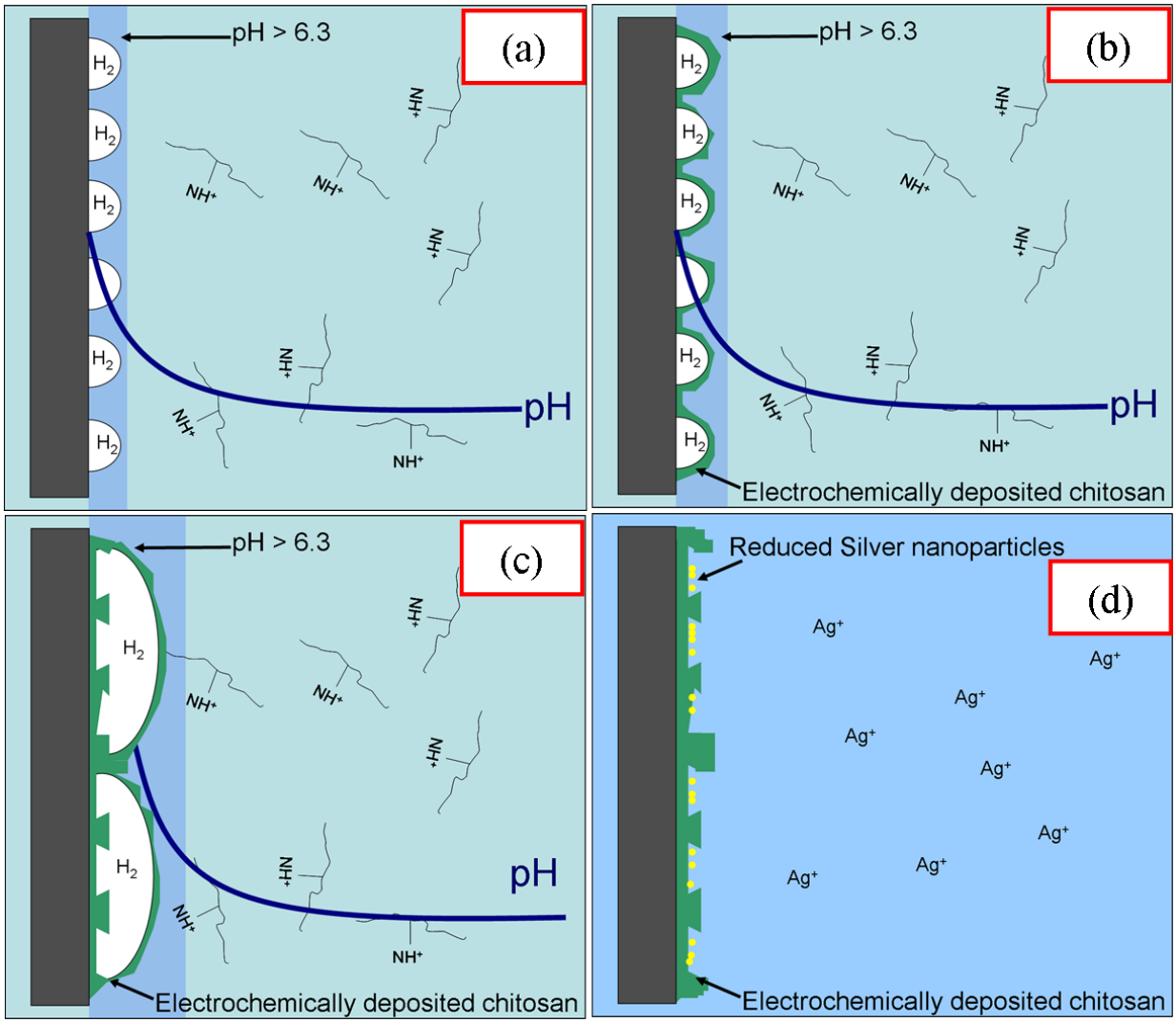

Table of Contents

List of Figures

Acknowledgements

I would like to express my most sincere gratitude to my supervisor, Prof. Gary P. Halada. He has provided great guidance and support throughout the whole period of my Ph.D. study in all aspects. His enthusiasm, his inspiration and his vision has kept me motivated. His encouragement, especially during testing times of low funds has enabled me to carry on the work rewardingly. The most important thing I have learned from him is importance of being nice with everyone, in long run it does pay off.

Many thank to Prof. Chad Korach, Prof. Brian Phillips, Prof. James Kubicki and Prof Scott McLennan for extremely beneficial collaborations during my study. Special thanks go to Prof. Chad Korach for being as external member in my committee.

I am very grateful to Prof. Dilip Gersappe for all the help he has provided as graduate program director and for being chairperson of my defense committee. Special thanks to Prof Yizhi Meng for agreeing to be on my committee at last minute. I would also like to thank Prof. Jonathan Sokolov, as my preliminary examination committee member, his valuable insights played a very important role in solidifying my research focus.

I would also like to thank Dr. Jim Quinn for helping with experiments anytime I needed, even on weekends. Finally I would like to state that I spent a great life during my Ph.D. study. Appreciation is expressed to all my past and current friends from department, Dr. Samrat Chawda, Dr.

Jose Mawyin, Dr. Atin Sherma, Dr. Dong Han, Katarzyna Sawicka, Michel Cuiffo, Chris Young, Joseph Ortiz and Ganan Jodhani to name a few, and many friends outside the department including but not limited to Pranav Nawani, Gajenrda Pandey, Anand Kashyap and Ashish Verma and of course my brother Ayoosh Jha.

I acknowledge the support provided by the National Science Foundation through contract number CHE0221934.

Chapter 1:Background

Interactions between metals and non metals, including organic ligands, are vital to our very existence from oxygen carrying capacity of hemoglobin imparted by iron and photon absorbance of chlorophyll containing magnesium to enzymes containing cobalt, zinc etc. Even without the knowledge of bonding, metallic ions bonded with non-metallic ligands (coordination compounds) have been utilized by civilizations for thousands of years. The first known use of coordination compound is bright red colored alizarin dye first used in India. Over the course of centuries many organic based as well as fully inorganic (using ammonia etc.) coordinated compounds were synthesized mainly for dyes and pigments application. Early compounds and theories of coordination chemistry are well documented by Joan Gispert in the book “Coordination Chemistry” [1].

The concept of metal complexes as we understand it now was first introduced by Alfred Werner in 1893 to explain the amount of silver chloride deposited by different Cobalt (III) chloride with ammonia. Over the years many theories have been developed to explain optical magnetic and electronic properties of coordinated compounds including molecular orbital theory, crystal field theory and ligand field theory. For a detailed information on development of various theories in 20^{th} century “The Chemical Bond: Structure and Dynamics” edited by Ahmed Zewail [2] is

highly recommended. In about a century since its invention coordination chemistry has come to occupy the center of chemical world due to its widespread applications in the fields of medicine, biochemistry, organometallic chemistry and catalysis.

Perhaps the greatest transformation in our world by coordination compound has been their catalytic application in polymerization. Since the discovery of Ziegler-Natta catalysts in 1950s billions of pounds of polyolefins alone have been synthesized [3] and thousands of patents have been filed [4] for different catalysts in polymerization. With the abundant supply of organic molecules from the coal and petroleum industry as well as advances in catalysis, polymers with controlled size, chemistry and properties had been synthesized and became integral part of civilization within 50 years by the end of 20^{th} century.

The 20^{th} century also saw exponential growth in demand for metals. In the USA alone demand for metal and minerals grew from about 160 million tons in 1900 to 3.3 billion tons by the end of century [5]. The extensive mining, processing and use of metals have led to their release into the environment. While some metals like aluminum and iron are benign, many metals including lead, mercury, arsenic, chromium and uranium are serious health hazards [6]. Complexation of these elements with natural organic matter in soils plays an important role in their transport and bioavailability. With an ever increasing focus on the environment since 1960s more and more studies have been directed

towards understanding metal-organic interaction from the point of view of remediation.

The next quantum leap in coordination chemistry came with the development of nanotechnology. Nanoparticles are giant pseudomolecules with complex internal structure and high surface energy. Small size and high surface energy give metallic nanoparticles unique features differentiating them from their bulk counterparts. The surface of nanoparticles is ubiquitously coated with lighter molecules which can alter its properties like optical characteristics, solubility and stability [7]. Large surface area offered by nanoparticles coupled with the flexibility in properties of nanoparticles attached to tailor made ligands have led to great deal of interest and extensive application of nanotechnology in various fields, including the most pressing one of our times, energy.

From catalytic converter in automobiles to dye synthesized solar cells and from supercapacitors to fuel cells no sphere of energy research has remained untouched by metal-organic interactions in nanoscale. Arguably the most pronounced effects have been witnessed in fuel cell technology: the adsorption of fuel onto electrode surfaces, oxidation of fuel on catalytic surfaces, charge transfers between electrolyte and electrode as well as reduction of oxygen are all based on metal-ligand interactions. Consequently a large volume of research in recent years has been directed at better understanding metal-ligand interactions in nanoscale and improving their performance and application.

1.1. Hypothesis of current work

The research reported in this thesis will improve our understanding of metal ion-organic ligand interactions during chemical and electrochemical processes, and in particular will explore the following concepts:

Intentional or unintentional (natural) association of reactive metal ions or oxyions with organic ligands results in the formation of nanoscale structures. In some cases, the structure consists of organic colloids, as in the case of polycondensation catalyzed by metal ion contaminants. In other cases, the metal ions themselves can be reduced, resulting in the formation of nanoparticles.

In all cases, the organic ligand can remain somewhat weakly associated with the metal through outer sphere complexation or hydrogen bonding. Where association of the organic ligand with the metal ion is stronger discreet nanostructures cannot form, and the association remains on a molecular scale.

By controlling the nature and reactivity of organic ligands (whether through pH or chemical modification), the resulting nature of the end state of the association (resulting in either strongly bound and hence dispersed chemical association or discrete nanostructures) is controlled for engineering applications (remediation, nanomaterial formation, etc.)

Further, by controlling the kinetics of the reactions in the metal ion-organic media through localized control of pH, electron transfer processes and other processing parameters, the physical characteristics as well as chemical stability of the resulting nanostructures can be controlled.

Chapter 2: Interactions of uranium with organic molecules.

2.1 Introduction

Uranium is present in our environment due to its natural occurrence, mining, processing and subsequent use. Radionuclides from mill sites, nuclear facilities and waste disposal sites can be spread by air and groundwater which necessitates the study of uranium transport and reactions in the environment: a number of such studies have been conducted [8-15]. Many factors affect the speciation and transportation of uranium in soil and groundwater including minerals in soil, nature and amount of organic matter in soil, pH of soil and water, rate and direction of groundwater flow, and hydraulic gradient [16]. Contaminant uranium in the subsurface has been found in very diverse forms including as uranyl phosphate, uranyl hydroxide, and an ill-defined uranyl organic phase at Fernald [17]. In studies conducted at Oak Ridge National Laboratory, uranyl has been found to exist complexed with phosphates and carbonates, associated with iron and manganese phosphates [8], and complexed with soil organic matter [18].

Humic substances form the majority of natural organic matter (NOM) in soil. Humic substances are high molecular weight, naturally occurring complex aggregates of aliphatic and aromatic chains having a number of common functional groups. Humic substances interact with metal ions through functional groups, forming soluble complexes, precipitating metal

ions by reduction or by ion exchange, modifying the sorption behavior of mineral surfaces towards metal ions and modifying colloidal particles containing metal ions [19]. More than 40 binding sites for complexation have been reported for humic materials including carboxylate, carbonyl, polyphenolic and amine functional groups [20]. Oxalic acid is simplest aliphatic molecule with two carboxyl group making is highly acidic and an ideal analogue towards understanding humic materiel-metal interaction. Catechol (o-diphenol benzene) is the simplest aromatic molecule containing highly reactive diphenol groups similar to many larger polyphenols constituting humic material, which makes catechol an ideal candidate for study of metal ion association relevant to contaminant mobility in soils. Due to its common presence as a functional group in NOM, catechol is also an ideal candidate for the study of oxidative polymerization [21]. Oxidative polymerization is an important process to understand because of its role in humic polymers originating from decomposition of plant residue [22].

In addition to the relevance of using catechol as a model ligand to understand reactions of mobile metal ions with subsurface organic constituents, catechol itself in the subsurface originates from both natural and man-made sources. It is produced in nature by bacterial degradation of plants and animals [22]. Catechol and other phenolic compounds are produced by many chemical industries and need to be removed from wastewater discharged by those industries [23]. While catalytic

polymerization of catechol was first demonstrated by Ziechmann using silica [24], it has also been observed using alumina, FeO, MnO,Ag_2O, soil, silver colloids [21] and various enzymes, including laccase [23], horseradish peroxidase and soybean peroxidase [25]. These enzymes, along with an oxidizing agent (hydrogen peroxide/dissolved oxygen), oxidize phenols to the phenoxy radical. In turn, the generated phenoxy radicals associate to form dimers, trimers and polymers [26]. Abiotic oxidative polymerization of phenolic compounds was investigated by Colarieti *et al.* al using soil samples, and it was established that both soil and dissolved oxygen are required for polymerization [27]. These authors later formulated a three step mechanism for abiotic oxidation of catechol: (1) catechol is oxidized by metal oxide(Fe and Mn oxides) and the metal oxide is reduced (2) complexation occurs between the reduced metal and remaining catechol, and (3) the metal-catechol complex is oxidized by dissolved oxygen to form polymers [28].

In this study we have investigated uranyl (UO_2^{2+}) interactions with catechol using spectroscopic techniques including Raman, FTIR and UV-vis spectroscopies. Catechol was found to polymerize in the presence of uranyl. Catechol polymerization was further investigated for effects of pH and dissolved oxygen and presence of other oxyions. Molybdate was used for comparison as it is well known oxidizer, and molybdenum is a known catalyst for benzene hydroxilation [29]. Moreover, molybdenum occurs naturally with uranium and is present in the form of MoO_4^{2-} in leach

solutions generated during hydrometallurgical extraction of uranium [30]. Molybdenum is also present in spent fuel rods formed by fission of uranium and beta decay of niobium, where it is found that Mo^{6+} converts to MoO_2^{2+} under oxidizing condition with an ionic potential similar to UO_2^{2+} [31]. For these reasons as well as the fact that molybdenum itself is a contaminant in groundwater [32] makes molybdate an ideal candidate for comparison with uranyl.

2.2 Experimental

2.2.1 Synthesis of complexes

0.1M aqueous solutions of catechol (o-dihydroxybenzene, Aldrich chemical Corp.), uranyl nitrate (Analar, BDH Chemicals Ltd.), Oxalic acid (ethanedioic acid, Fisher Scientific) and sodium molybdate (Aldrich Chemical Corp.) were prepared by dissolution in DI (>18MΩ/cm) water. To obtain complexes, catechol was added to uranyl nitrate and sodium molybdate in 1:1 volume ratios. Oxalic acid was mixed with uranyl in 1:1 and 1:2 molar ratio. All the solutions as well as 1:1 molar ratio complexes were adjusted to 2, 4, 6, 8, 10 and 12 pH using 1M and 0.1M NaOH and HCl solutions. Oxalic acid uranyl complexes were adjusted to pH 3, 7 and 10 to explore the interactions in acidic, neutral as well as basic environment. The pHs of solution were measured using a Corning Scholar 425 pH meter. Solutions and complexes were analyzed using UV-Vis, Raman and IR-ATR spectroscopy. Spectra of solutions of uranyl nitrate and sodium molybdate at various pH were taken before spectra of uranyl-

catechol and catechol-molybdate to distinguish effects of complexation from the effect of pH change.

2.2.2 Fourier transform infrared spectroscopy (FTIR)

A Nicolet Model Magna 760 FTIR spectrometer with a ZnSe ATR crystal was used for analysis. Solutions containing complexes were placed on the crystal (in their liquid state). A 4cm^{-1} resolution was used and 256 scans were averaged to improve the signal-to-noise ratio. The range selected for data acquisition was 3000-900 cm^{-1} (below 900 cm^{-1} noise was too high for meaningful signal to be observed). DI water (>18MΩ/cm) was chosen as background to minimize signal from water peaks during data collection.

2.2.3 Raman spectroscopy

A Nicolet Almega dispersive Raman spectrometer with a 785 nm laser source was used for analysis. Samples were put on a gold slide as droplets and the Raman microscope was focused at the gold-solution interface. Data from averaging 256 scans in the 3444-108 cm^{-1} range was collected. OMNIC for Nicolet Almega software version 7.3 was used to process data.

2.2.4 UV-Vis spectroscopy

UV-Vis measurements were taken using an Ocean Optics S2000 spectrometer and OOIBase32 operating software. For UV-Vis

measurements 1mM samples were used; deionized water was used as reference spectrum. Spectra were collected with 80 mSec integration time with an average of 10 measurements.

For anaerobic UV-Vis measurements 1mM catechol solution was deaerated by bubbling nitrogen through the solution for four hours. NaOH pellets were then added to solution until pH was greater than 12 while the solution continued to be deaerated with nitrogen. This anaerobic catechol solution at high pH was then transferred to a quartz cuvette and which remained capped for the initial measurement: for subsequent readings the cap was removed to allow air to interact with the solution.

2.3 Results and discussion

2.3.1 Impact of pH on uranyl nitrate and sodium molybdate

FTIR analysis (figure 2.1) of uranyl nitrate at different pH shows a shift to lower wavenumbers of the peak associated with the U=O antisymmetric stretching frequency of uranyl with an increase in pH, shifting from 961 cm^{-1} at pH 2 in solution to 942 cm^{-1} in the precipitate formed at pH6. On further increasing the pH the signal became lost in the background noise.

The observed shift is likely due to the presence of a greater number of hydroxyl ions coordinated with the uranyl ion, due to of the formation of different uranyl hydroxides at different pH. In general there are more than 20 uranyl oxide hydrates [38] which may be formed at elevated pH. Uranyl

hydroxide was found to have precipitated out of solution at high pH as indicated by the disappearance of the uranyl peak in spectra from solution at pH 6 and its subsequent appearance in the condensate. Raman analysis (figure 2.2) showed similar results: there is a significant decrease in stretching frequency of the U=O uranyl peak from 875 cm^{-1} at pH 2 to 794 at pH12 (observed in solution up to pH4 and in precipitate from pH6-12). This decrease in frequency is a known indicator of complexation, and indicates the presence of various uranyl hydroxides [39]. Samples were stored in closed containers limiting the amount of atmospheric carbon dioxide absorption by solution to avoid formation of uranyl carbonate. No peaks corresponding to uranyl-carbonate (1117 cm^{-1}), even at high pH, were found.

Raman spectra from the molybdate solution (figure 2.3) also show a shift in the peak associated with the Mo-O vibrational frequency in molybdate from 960 to 902 cm^{-1} with increase in pH, but the change in frequency with pH is not gradual as in the case of the uranyl peak. The peak at 960 cm^{-1} starts to lose intensity for pH greater than 4 while a new peak at 902 cm^{-1} gains intensity to pH6: there is no peak at 960 cm^{-1} at pH8 and above. This shift is due to the fact that molybdate structure changes with pH in basic and neutral solutions: it normally exists as simple tetrahedral molybdate ion, but at pH lower than 6 it exists as heptamolybdate $[Mo_7O_{24}]^{6-}$. This transition is complete at pH4.5 [40].

2.3.2 Polymerization of Catechol at Elevated pH

The 0.1 M catechol solution was found to become increasingly opaque with increasing pH. The solution first became brown in appearance at pH6 and, on further increasing the pH to 8 or higher, it turned black (figure 2.4). UV-Vis spectra of the solutions show a peak in the range of 250-300nm at all pHs: this is characteristic of π-π* electron transitions in phenolic compounds [33]. The change in color of the catechol solution was found to be associated with a bathochromic shift and an increase in intensity in the UV-Vis absorption spectra indicating a greater degree of π-conjugation and thus polymerization [34,35,36] (figure 2.5). A new peak ~320nm emerges at higher pH indicative of formation of a higher molecular weight polymer at higher pH [37, 33].

Dissolved oxygen was found to play a role in polymerization, since in absence of oxygen no change in color associated with polymerization was observed even at pH as high as 12. In addition, the UV-Vis peak at 320nm is initially absent (figure 2.6, t=0). The peak slowly emerges as air is allowed to interact with the solution and can be clearly seen after four hours (figure 2.6, t=240).

FTIR analysis (figure 2.7) of the catechol solution at pH 2 and pH 12 shows clear evidence of the formation of polycatechol. The four absorption peaks between 1466 and 1515 cm^{-1} may be attributed to aromatic ring C=C vibration bands characteristic of the benzene ring.

Peaks at 1277 and 1260 cm^{-1} are due to C-O vibration[41]. The broad peak at 1600 cm^{-1} is a combination of C=C and substituted benzene ring vibrations. Peaks at 1202 and 1102 cm^{-1} observed at pH less than 6 are attributed to C-H in-plane vibrations. Analysis from the solution at pH 12 showed C=C vibration bands between 1410-1584 cm^{-1}, consistent with the formation of polycatechol. The peak at 1487 cm^{-1}, found to appear at pH higher than 8 is attributed to substituted benzene ring vibrations (which is indicative of catechol chelation and/or higher substitution). In addition, peaks associated with C-H vibrations were not found in the pH 12 solution.

Raman analysis (figure 2.8) of catechol at different pH is also consistent with the formation of polycatechol. The spectra for lower pH (2,4,6) solution show in-plane and out-of plane CH deformation bands at 1040 and 774 cm^{-1}. These peaks are absent at higher pH (8, 10, 12). A new peak associated with the phenoxy radical appears at 1494 cm^{-1}. New peak at 1382 cm^{-1} associated with in plane C-H rocking vibration was also observed indicating retention of some C-H bonds in polycatechol . In addition, a new peak was observed at 1584 cm^{-1} indicating formation of Tropones. From this evidence it appears polymerization is taking place by formation of C-C bonds between benzene rings following deprotonation of catechol. Pk_a for catechol is 9.5; thus at pH 8, approximately 3% of the catechol will be deprotonated, likely enough to start polymerization (figure 2.9).

2.3.3 Catechol complexes in the presence of uranyl and molybdate

Addition of uranyl ion to catechol solution was found to induce polymerization at a significantly lower pH than the pH required for polymerization in a pure catechol solution: the uranyl/catechol solution was found to become dark instantaneously at pH 6. FTIR spectra of the uranyl/ catechol solution (figure 2.10) shows proof of complexation by increase in intensity of the peak due to the substituted benzene ring at 1488 cm^{-1} as well as an increase in intensity of the peak associated with the C-O band at 1252 cm^{-1}. No major difference in spectra was observed between solutions of 1:1 and 1:2 ratio of uranyl:catechol. Raman spectrum (figure 2.11) from the uranyl-catechol solution confirmed polymerization at low pH: C-H bands at 1052 and 774 cm^{-1} were present only at pH2. The shift in the C=C peak to 1582 cm^{-1} as well as the appearance of the peak associated with phenoxy groups at 1497 cm^{-1} were observed at pH as low as 2.

By visual observation it appeared that sodium molybdate had a similar and more intense effect on catechol than uranyl nitrate, as color change was observed even at pH2 in fresh solution (as opposed to the requirement for a pH6 for the uranyl-catechol solution). Molybdate is capable of catalyzing polymerization at even more acidic pH due to its high affinity for aromatic o-dihydroxy compounds [42] A shown by the FTIR spectrum from the molybdate/catechol solution at pH 6 (figure 2.10),

the substituted benzene ring intensity at 1483 cm^{-1} increased accompanied by a larger increase in the C-O band at 1264 cm^{-1} than in the case of uranyl association with catechol at pH 6. The results indicate that oxygen substitution is much faster in presence of molybdate as opposed to uranyl at acidic pH. In the Raman spectrum (figure 2.11) from the molybdate/catechol solution, C-H bands were not present at any pH, and the C=C peak was shifted to 1563 cm^{-1} showing substitution and conjugation. The peak associated with Mo=O stretching in molybdate was also shifted from 900 to 932 cm^{-1} showing evidence of complexation with catechol.

In all cases, whether by pH-induced polymerization of pure catechol solution or whether catalyzed by uranyl or molybdate ions at lower pH, it seems the mechanism of catechol polymerization is by formation of C-C bonds between benzene rings and not by C-O-C bond formation, as characteristic peaks of benzyl ether1090 cm^{-1} were not observed in any case. Polymerization is associated with a high degree of substitution in the benzene ring as proposed by Arana *et al.* [43] and with formation of quinones [44]. No polymerization was observed under anaerobic conditions, which implies that substitution takes place before polymerization. Formation of quinones and substitution of H by OH may be facilitated by an alkaline environment.

Raman spectra of six month old uranyl/catechol solution were obtained to investigate the effect over time on complexation. All the

characteristic peaks of catechol polymerization were observed in aged samples even at pH as low as 2 (figure 2.11), whereas a pH of 6 was required for immediate polymerization. Polycatechol formed was found to have precipitated out of solution forming humic-like material. No uranium was found in the precipitate; all the uranyl remained in solution after the polymerization was complete. Hence the uranyl ion in solution acts as a catalyst for formation of polycatechol over time, even under quite acidic conditions by complex formation with oxygen from hydroxyl and quinone groups.

2.3.4 Oxalic Acid and its complex with uranyl

Raman analysis of oxalic acid (figure 2.12) at different pH shows no change in structure with change in pH. The peak at 1270 cm^{-1} is from C-O stretching of dimer carboxilic acid, while the peak at 1144 cm^{-1} is from C-O stretching of monomer. The peak at 1450 is a combination of C-O stretching and O-H deformation. 1351 cm^{-1} is O-H deformation of monomer. The band at 901 cm^{-1} is O-H..O out of plane deformation band for both monomer and dimer. 604 cm^{-1} represents C-O deformation band of dimeric carboxilic acid and 552 $cm^{-1}$is C-O out of plane deformation vibration. The results show that oxalic acid exists as a mixture of monomer and dimer at all the pH investigated.

Raman spectrum of uranyl oxalic complex (figure 2.13) shows shift in uranyl peak from 873 to 857 cm^{-1} on addition of oxalic acid to uranyl

nitrate solution at pH3 showing evidence of complexation similar results were found for neutral and basic pH also. While no change was observed with changing metal-legand ratio at acidic pH, on comparing condensate and supernatant solution formed at basic pH we see the effects of relative amounts of uranyl and oxalic acid. In the condensate formed at 1:1 no oxalic peaks are present (figure 2.14) but when uranyl and oxalic are added in 1:2 ratio, oxalic acid peaks are present in condensate. In the solution no uranyl peak are detected at 1:2 ratio (figure 2.15). A possible explanation of the phenomenon can be that there exists a dynamic equilibrium between oxalic acid, uranyl-oxalate complex and uranyl hydroxide, which on addition of excess oxalic acid is shifted to right and hence the amount of uranyl-oxalate in solution is reduced. The results prove that uranyl ion forms strong complex with oxalic acid at all pH and the solubility of uranyl increases upon association with oxalic acid.

2.4 Conclusions

Presence of organic matter in environment can significantly alter mobility of uranium, while complexation with large molecules reduces the mobility complexation with small organic acids can increase solubility and hence transport and bioavailability of uranium.

In presence of uranyl ions, polymerization of catechol was observed even at pH2 over time which can be due to complexation of catechol by uranyl ions with subsequent transfer of electron density from the benzene

ring towards uranyl, hence facilitating removal of H (figure 2.16). This is consistent with observations by Horsman for catechol polymerization catalyzed by Fe(III) or by Arana for polymerization catalyzed by $CuO\text{-}TiO_2$ [45,46]. Polymerization of catechol may also be influenced by the formation of a localized zone of high pH generated by abstracting protons from the salvation [48] shell present around uranyl ions. Recent collaborative work with Kubicki, et al., indicates the inclusion of not only a primary but also a secondary salvation shell of from 20 to 30 water molecules is necessary for accurate quantum mechanical molecular modeling for uranyl-organic ligands, including uranyl-catechol [47].

While further study is needed for developing accurate models of the kinetics of long term uranyl association with aromatic molecules with phenolic ligands, this result has a number of significant implications. These include (a) understanding uranium sorption and transportation in surface and some subsurface environments (b) Optimizing the operation of any remediation process which either uses organic ligands or which is used to remove contaminant uranium from groundwater containing natural or pollutant organic material, and (c) for understanding the humification process through oxidative coupling of phenols, as this result shows that uranyl ion acted as catalyst in the process of polymerization with complexation acting as an intermediate step.

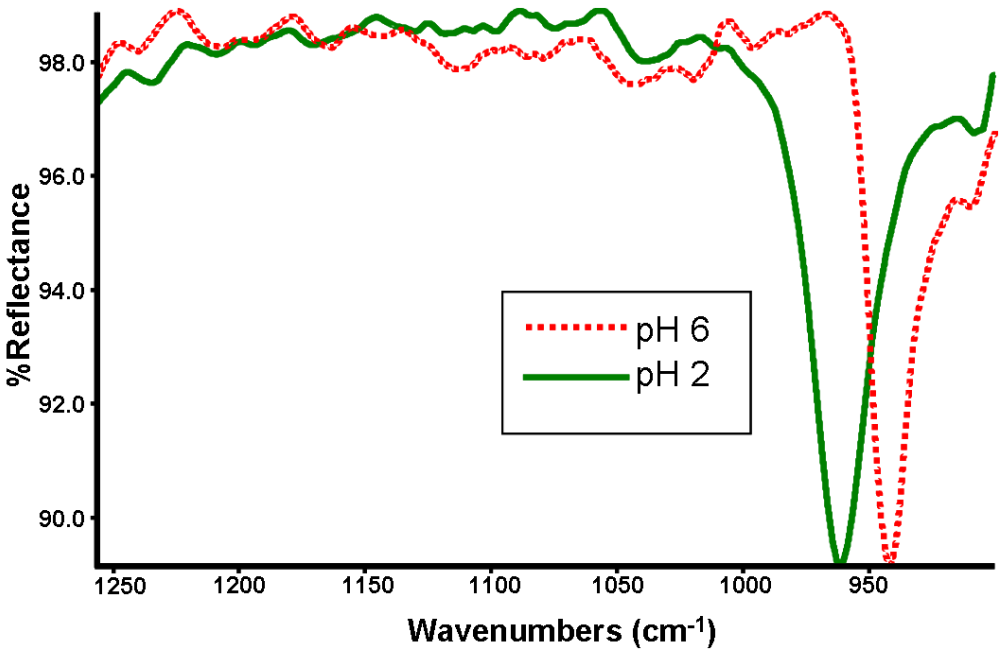

Figure 2.1 : FTIR spectra of uranyl ion in solution at pH 6 and precipitate at pH 6.

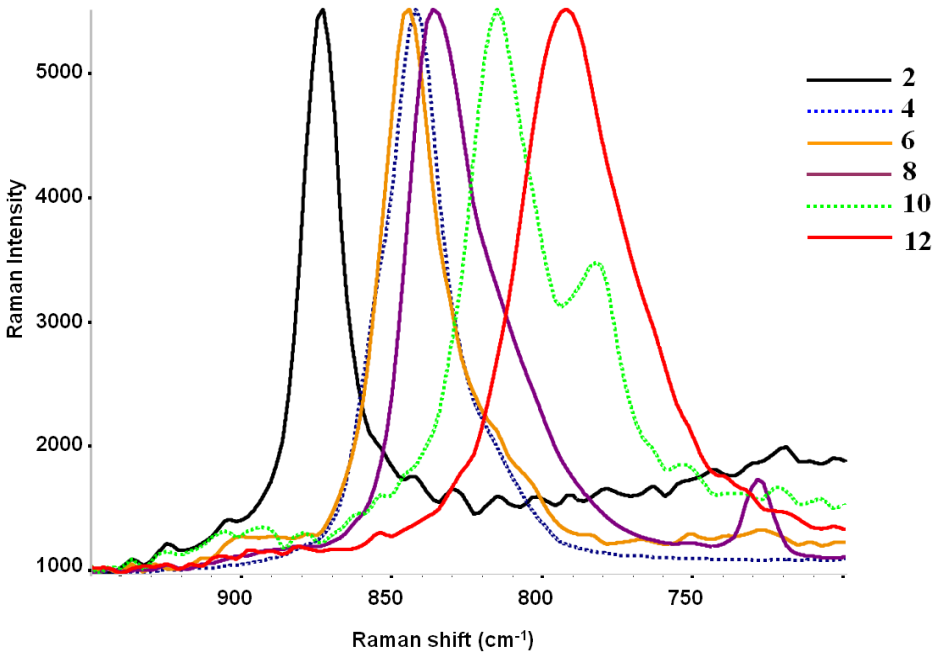

Figure 2.2 : Raman spectra of uranyl ion in solution at pH 2 and 4 and in the precipitate formed at pH 6, 8 10 and 12.

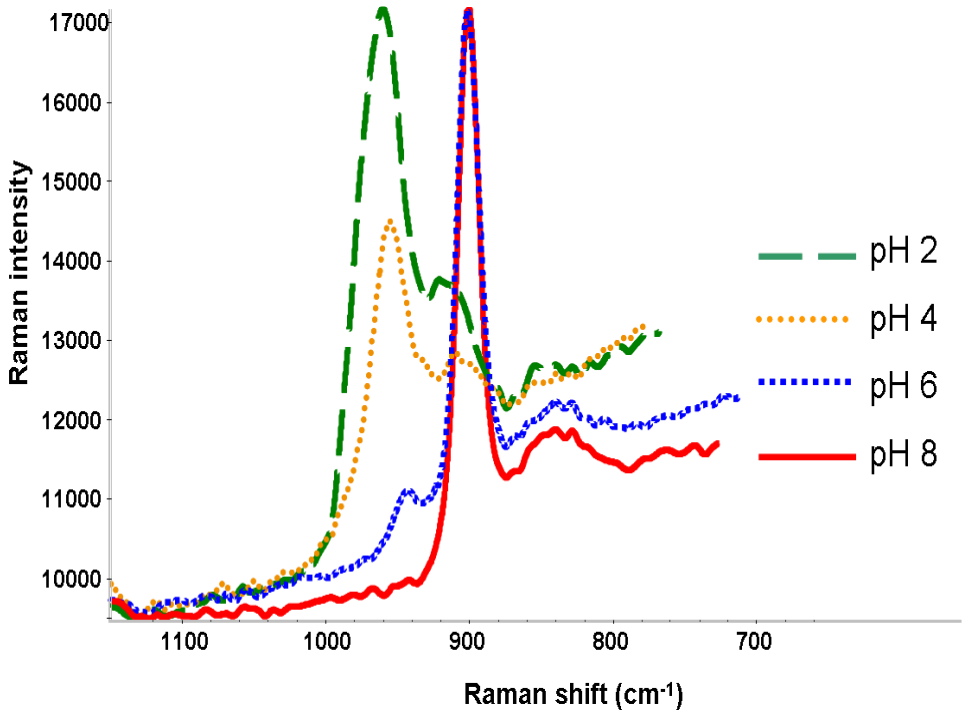

Figure 2.3 : Raman spectra of molybdate ion In solution at pH 2, 4, 6 and 8.

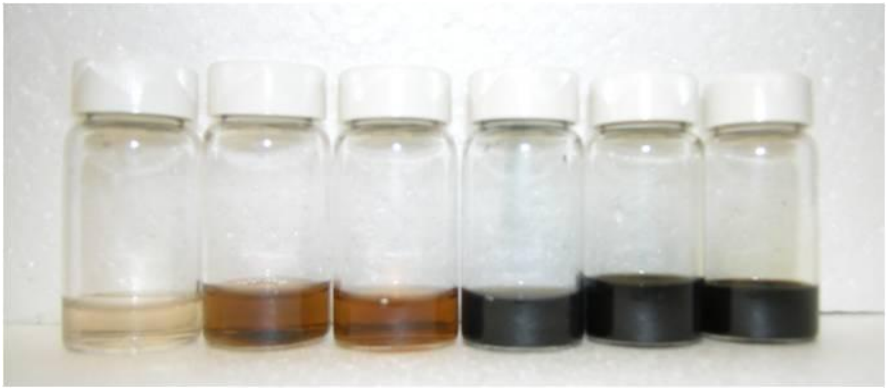

Figure 2.4 : Catechol solutions (0.1 M) at pH 2,4,6,8,10 and 12 (left to right).

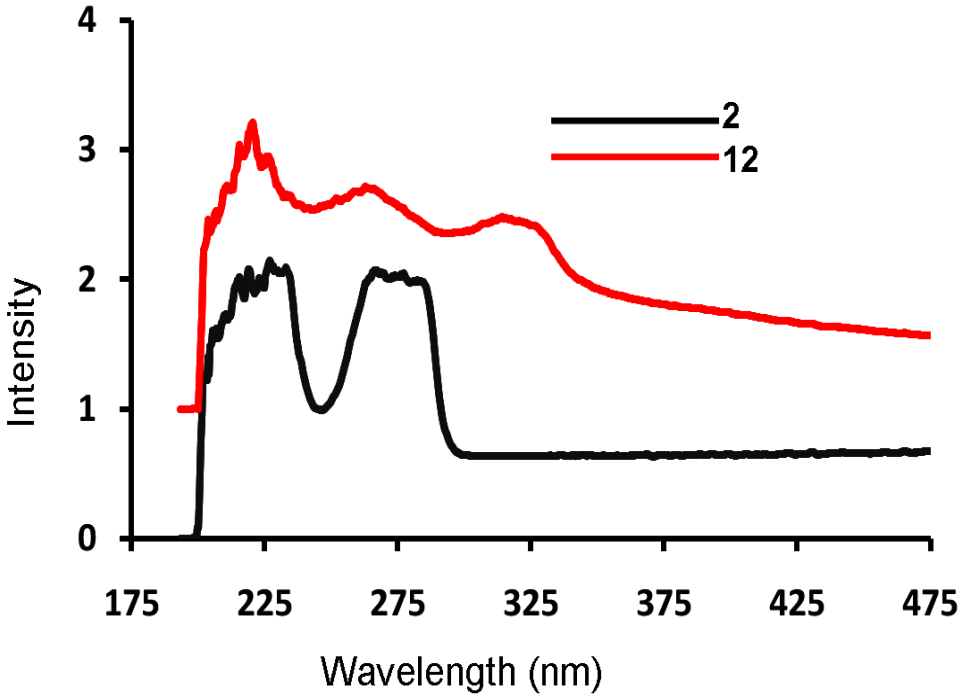

Figure 2.5 : UV-Vis spectra of catechol solution at pH 2 and 12.

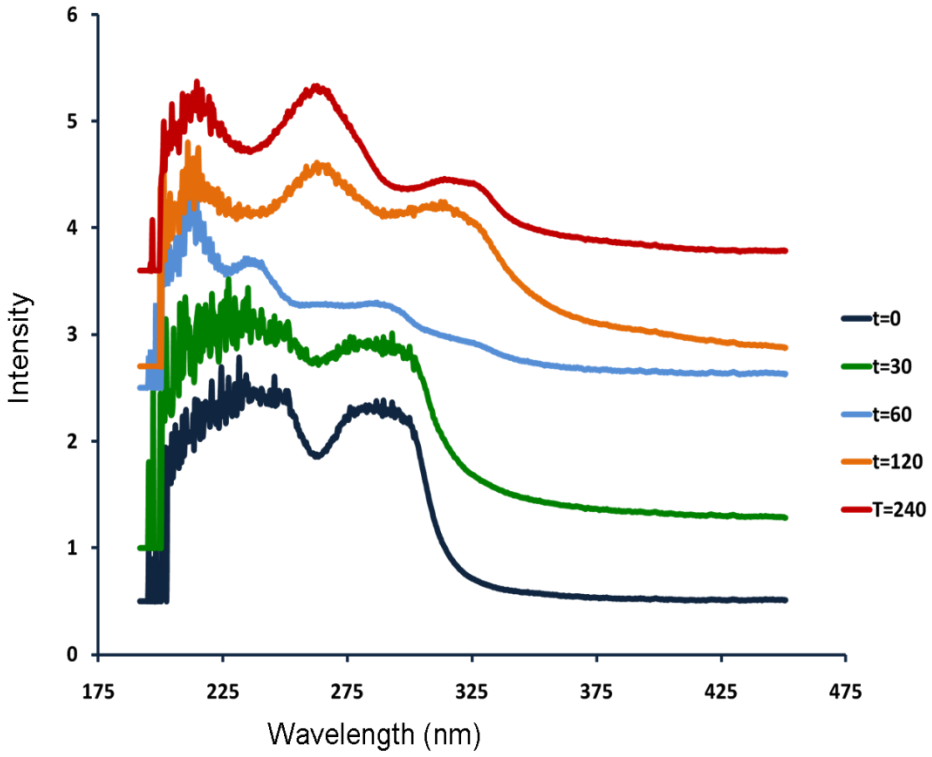

Figure 2.6 : UV-vis spectra showing polymerization of catechol in solution at pH 12 with exposure to air with time.

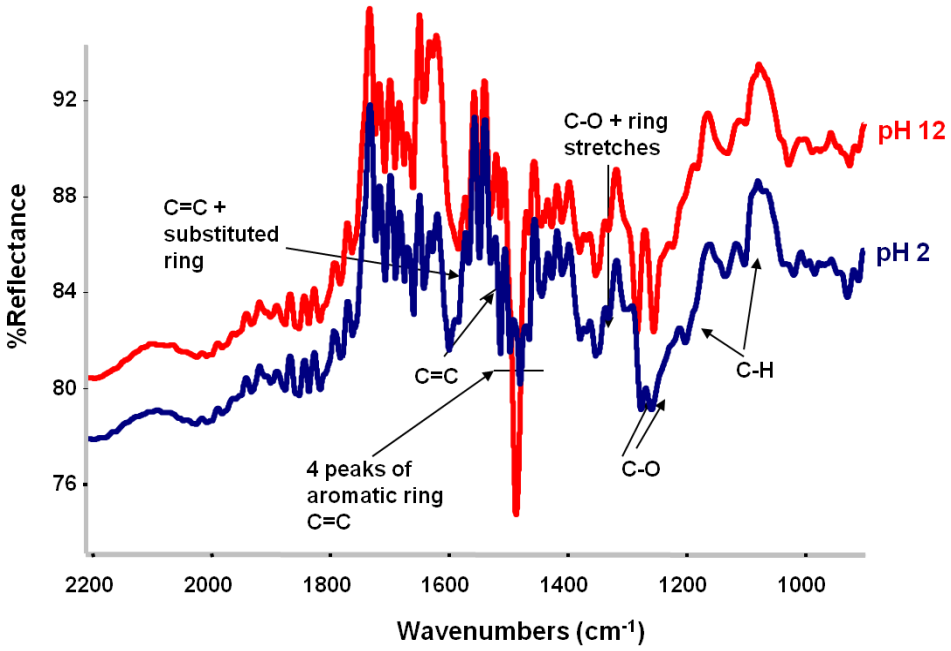

Figure 2.7 : FTIR spectra of catechol (pH 2) and polycatechol (pH 12).

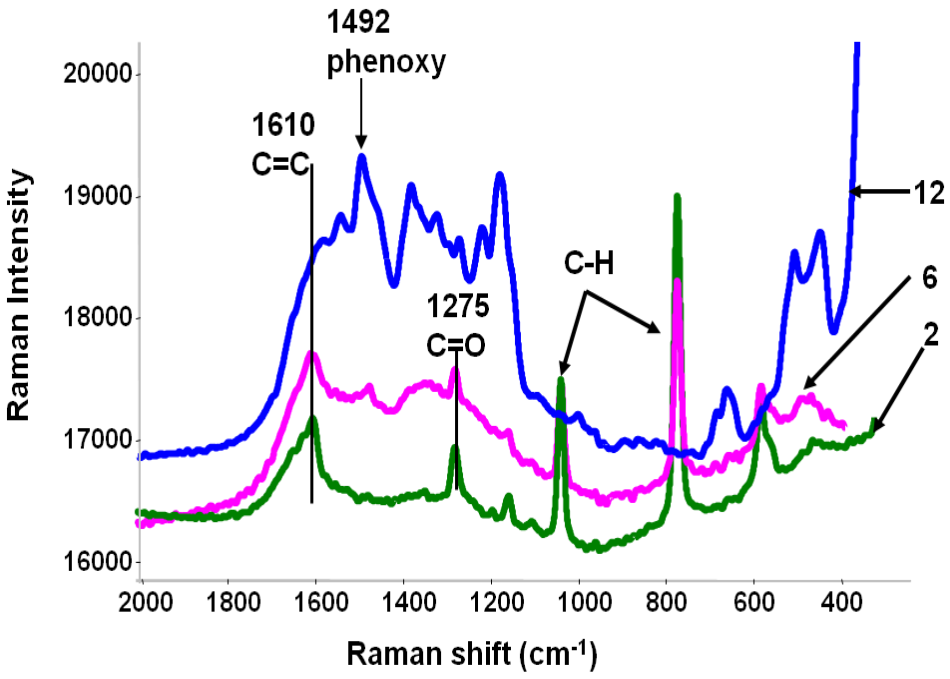

Figure 2.8 : Raman spectra of catechol and polycatechol at Ph 2, 6 and 12.

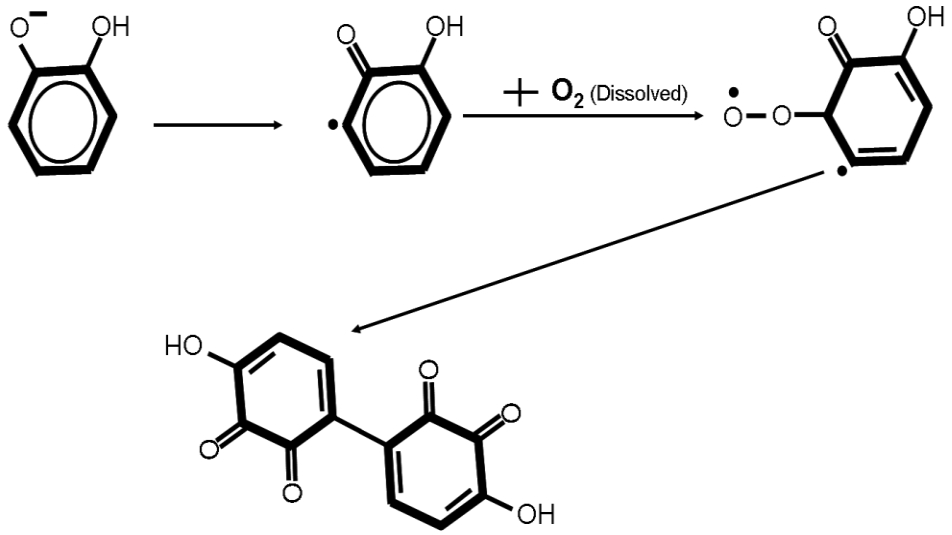

Figure 2.9 : Proposed mechanism of catechol polymerization at high pH.

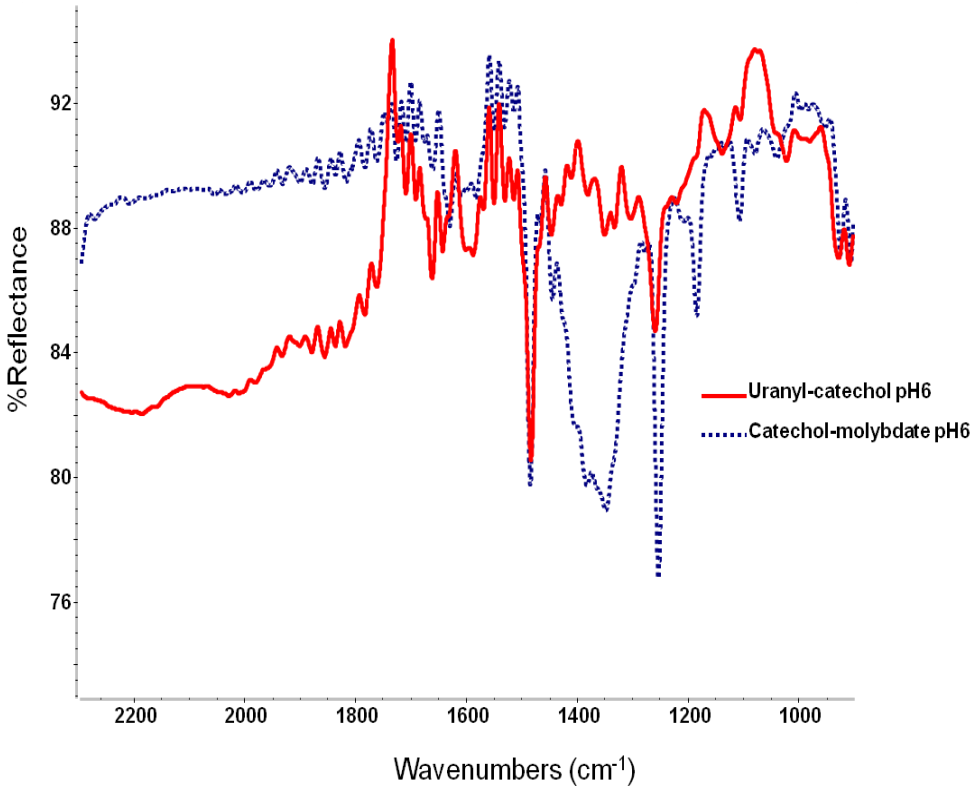

Figure 2.10 : FTIR spectra of 1:1 uranyl-catechol and 1:1 molybdate-catechol complexes at pH6

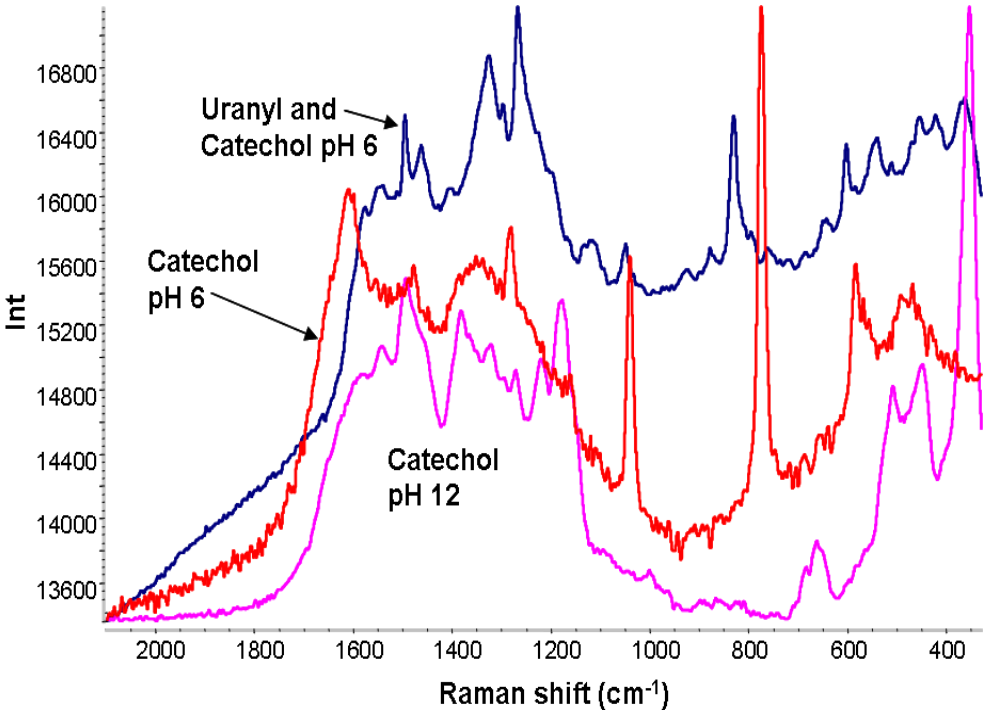

Figure 2.11 : Raman spectra of 1:1 catechol-molybdate at pH6, six month old uranyl-catechol at pH 2 and uranyl-catechol complex at pH 6.

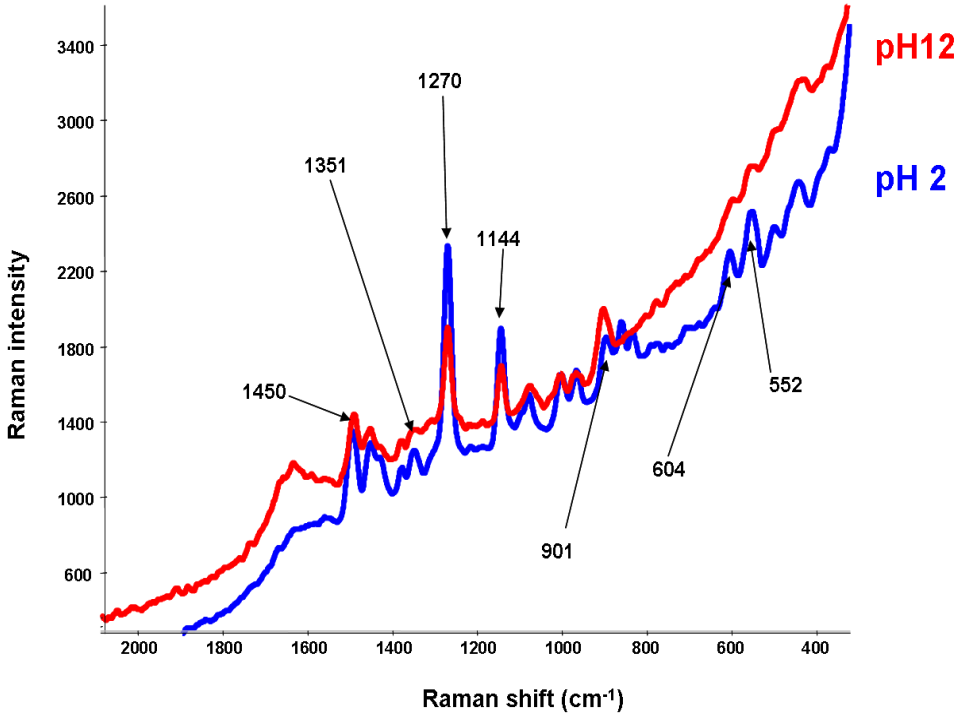

Figure 2.12 : Raman spectra of oxalic acid at pH2 and pH12.

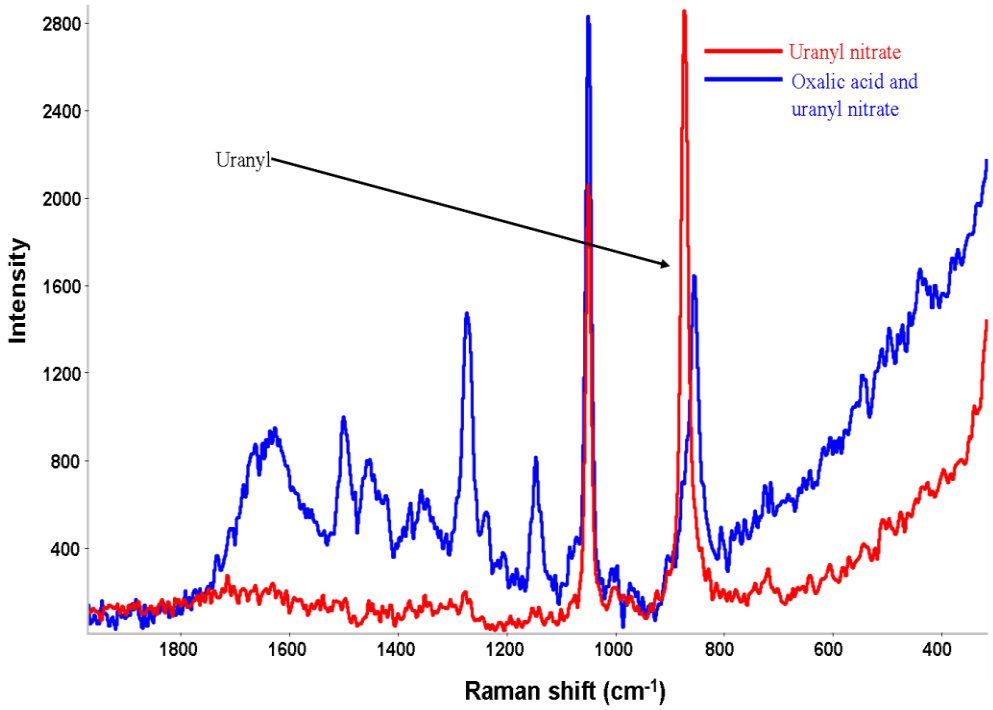

Figure 2.13 : Raman spectra of oxalic acid and uranyl-oxalate complex at pH2 showing proof of complexation.

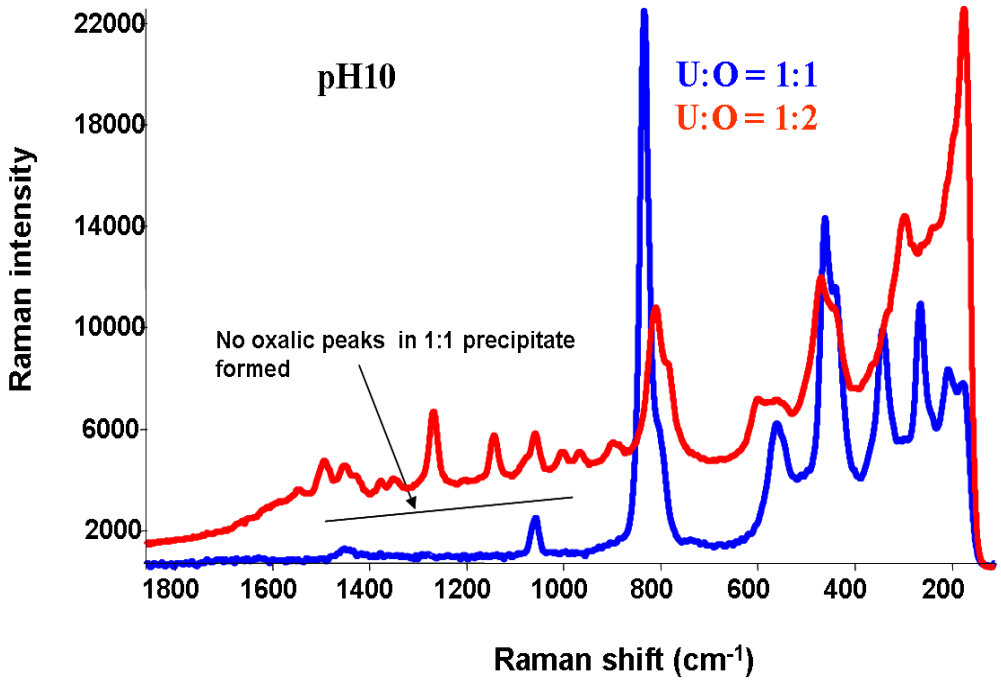

Figure 2.14 : Raman spectra of precipitate formed of uranyl-oxalate complex at molar ratio of 1:1 and 1:2 at pH10.

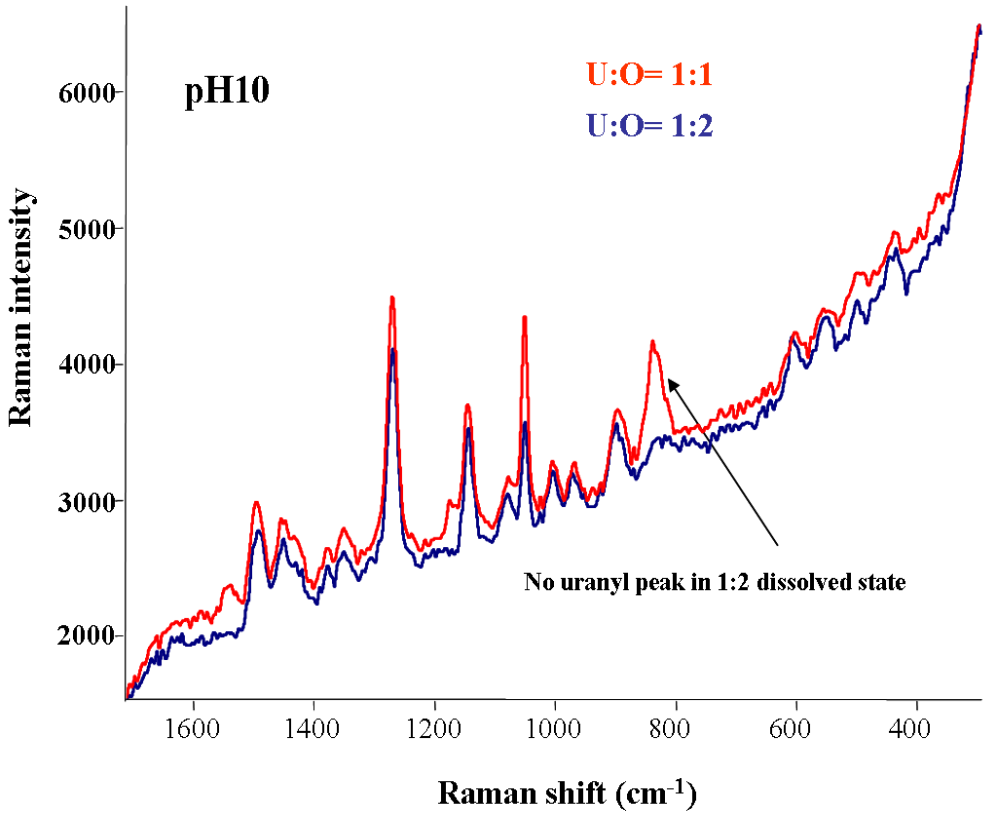

Figure 2.15 : Raman spectra of supernatant solution of uranyl-oxalate complex at molar ratio of 1:1 and 1:2 at pH10.

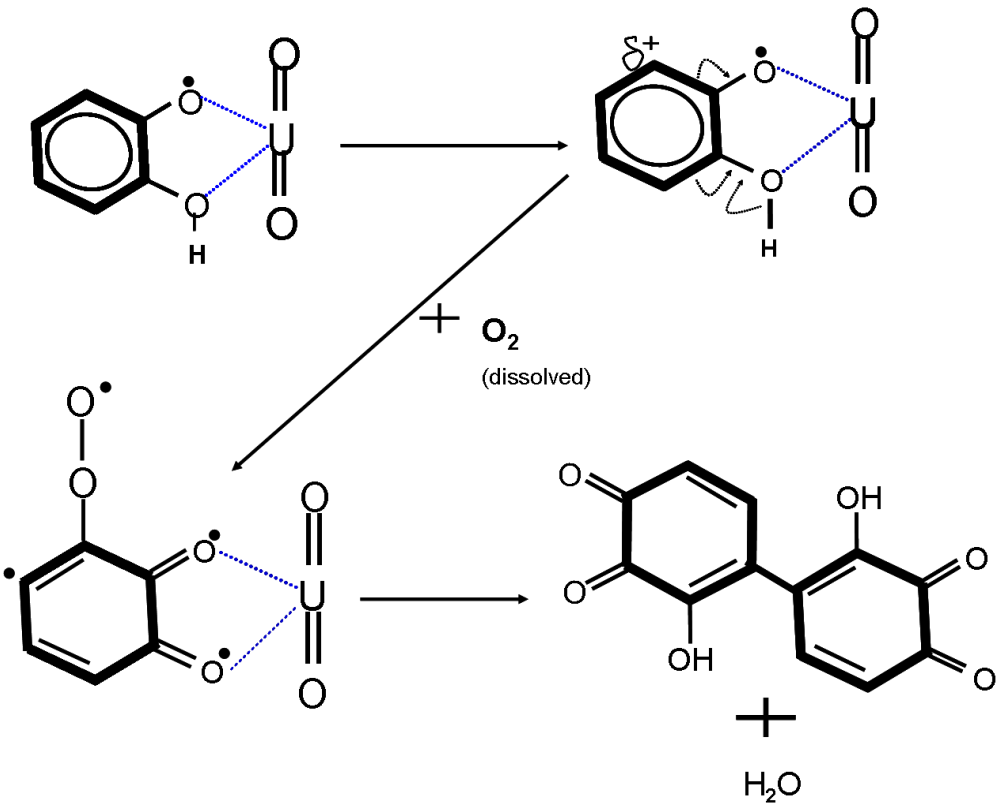

Figure 2.16 : Proposed mechanism of catechol polymerization in presence of uranyl.

Chapter 3 : Electrochemical modifications of Chitosan and their application in environmental remediation

3.1 Introduction

Heavy metal contamination of soil and groundwater is a major environmental threat. Contamination from toxic heavy metals is present in as many as 63% of 1200 sites on the National Priority List of the U.S. Environmental Protection Agency (EPA) for treatment of contaminated groundwater. At 11% of these sites chromium was found to be present making it one of the main heavy metal contaminants [6]. Chromium is used in industrial processes such as metal plating, leather tanning and pigment production resulting in release to groundwater [49]. In aerated aqueous solutions chromium is stable only as Cr(III) and Cr(VI) [50]. While Cr(III) is essential for living beings in small amounts for its role in carbohydrate metabolism[51], it is toxic at higher concentrations. Also, in alkaline environments Cr(III) can oxidize to Cr(VI), which is toxic even at low concentrations, as it induces coetaneous allergies and becomes carcinogenic over long periods of exposures [51,52].

Various methods developed for removal of heavy metals from groundwater include: isolation and containment, mechanical separation, pyrometallurgical separation, chemical treatment, permeable treatment

walls, electrokinetics, biochemical processes, phytoremediation and soil flushing [6]. Chemical remediation using naturally occurring biodegradable biomass has generated a great deal of interest due to its low cost and high efficiency [53]. Some of the sorbents based on biomass are bark, seaweed, leaf mould and chitosan; detailed information on these and a comparison of their chemistry and performance can be found in work of S.E. Bailey et al [54]. Chitosan is among the chief biomass-based remediation agents.

Chitosan is a linear, high molecular weight, crystalline polysaccharide consisting of β-(1→4) linked N-acetyl-D-glucosamine [55]. It is produced by alkaline N-deacetylation of chitin, the second most abundant natural polymer after cellulose [56]. Changing the acetamide group to amine increases the reactivity rendering chitosan a better chelation and adsorption agent than chitin[57]. The adsorption capacity of chitosan has been further enhanced using physical modifications including conditioning as gel beads and microcrystalline chitosan as well as chemical modifications such as cross-linking and insertion of new functional groups [58]. Chemical modification of chitosan utilizes the presence of primary amine and primary hydroxyl as well as secondary hydroxyl groups in the chitosan molecule, which makes it very amenable to further fictionalization and modification. Chemical modifications of chitosan have been thoroughly reviewed by Mourya and Inamdar [59].

In this section a novel electrochemical process followed by

photochemical treatment for chitosan modification is reported. The process results in formation of nitro groups through oxidization of a fraction of the amine groups of chitosan. The new biopolymer formed was characterized using spectroscopic techniques, and metal binding capacity was explored using chromium as chromate in aqueous solution. The adsorption capacity of the nitro-chitosan was compared with other forms of modified chitosan as reported in the literature.

3.2 Experimental

3.2.1 Electrodeposition of chitosan

The chitosan solution was made by mixing 1.5g low molecular weight chitosan (sigma Aldrich, 75-85%deacetylated) to 120ml DI water under constant stirring. 1M HCl was then added drop wise until all chitosan was dissolved, which was seen to occur as the solution reached a pH of 2. For electrochemical deposition of chitosan, polished type 304 stainless steel (metal composition approx. 19% Cr 9 % Ni, bal. Fe) was chosen as the working electrode. This process has been detailed by the authors in a previous publication [60]. Pt wire served as the counter electrode. A Gamry Reference 600 potentiostat was used to perform electrochemistry and Gamry Instrument Framework software was used for control and monitoring of voltage and current. Controlled potential coulometry at a voltage of -3.0 V (versus Ag/AgCl reference electrode) was applied for 5 minutes. The resulting hydrogel was rinsed in DI water to remove any chitosan solution entrapped in the resulting hydrogel. The gel was then

exposed to UV light (20W at 6 cm) for 10 minutes, following which it was then peeled from the electrode and left to dry further for 48 hours. A thin film may remain behind on the electrode surface, bound to the passive layer, as detailed in our previous work[60]. The dried gel film was then crushed mechanically to form powder for spectroscopic analysis and absorption experiments.

3.2.2 FTIR Spectroscopy

Fourier Transform Infrared Spectroscopy (FTIR) spectra were obtained using a Nicolet 760 infrared spectrometer modified to collect data in both mid- and far infrared regions. Samples were ground to a fine powder. Spectra were collected using an MCT-A detector with data resolution set to 2 cm^{-1} and summed over 256 scans to improve the signal-to-noise ratio. A Gemini sampling accessory (Spectra-Tech) collected diffuse reflectance data from powder samples. The analysis chamber was purged continuously with doubly dried air to prevent the absorption of water vapor, and a globar-type IR source was used.

3.2.3 Raman Spectroscopy

A Nicolet Almega dispersive Raman spectrometer with a 785 nm laser source was used for analysis. Powdered samples were placed on quartz slides and Raman microspectroscopy in reflectance mode was used for data acquisition. Data was collected in the 3600-400 cm-1 range. An average of 10 scans with 5s accumulation time for each exposure was

collected. OMNIC for Nicolet Almega software version 7.3 was used to process data. For comparison, chitosan solution at pH3 was dried (without any applied potential) on stainless steel and similarly analyzed.

3.2.4 X-ray photoelectron spectroscopy

To detect speciation of nitrogen, X-ray photoelectron spectroscopic (XPS) studies were carried out. Sample preparation consisted of peeling off the deposited film from stainless steel substrate after immersion in liquid nitrogen for one minute. The film was removed using a stainless steel razor and mounted on the XPS sample holder using indium foil. XPS measurements were performed using a custom-designed spectrometer that utilized a VG Scientific (Fisons) CLAM2 hemispherical analyzer with lensing, controlled by a VGX900I data acquisition system. An Mg $K\alpha_{1,2}$ (hv=1253.6 eV) X-ray source operating at 20 kV and 10 mA with a 20 eV pass energy was used at a pressure of 10^{-9} Torr. Measurements were taken at a 90° take-off angle with respect to the surface and charge correction was done by referencing to the C 1s line of adventitious carbon (284.6 eV).

3.2.5 Adsorption experiments

Stock solution (1000ppm) of Cr(VI) was prepared by using $K_2Cr_2O_7$ obtained from Sigma Aldrich, in deionized water (>18MΩ/cm) The stock solution was then diluted to give standard solutions of appropriate concentrations. Batch adsorption experiments were conducted in 250 ml

conical flasks and equilibrated using a magnetic stirrer. This is similar to the method used in references [50, 61] 0.02g of modified chitosan was added to 50ml of standard solution and equilibrated for 30mins. Supernatant solution was then filtered and analyzed. For equilibrium time determination, 0.5g of modified chitosan was mixed in 1l of 26ppm Cr(VI) solution under constant stirring. 2ml of solution was removed at predetermined times, filtered and analyzed. To determine the effect of pH on adsorption, pH of the 26ppm Cr solution was controlled using introduction of a small amount of 1M HCl and 1M NaOH solutions, while the remaining parameters were kept the same as that for the batch experiments. Chromium concentrations were measured using DCP-AES.

3.2.6 DCP-AES

Elemental analyses were carried out with an ARL Spectraspan VB Direct Current Argon Plasma Atomic Emission Spectrometer (DCP-AES). This system uses a Czerny-Turner spectrometer with an Echelle grating and 30° prism for order separation. At 400 nm reciprocal linear dispersion is 0.122 nm/mm and for a 25 microns entrance slit spectral band pass is 0.0030 nm. Analyses were performed in single element mode, using standard settings and a solution flow rate of 0.5 ml/min. Emission lines used for analyses were Cr 425-435nm.

Standards used for calibration for Cr analyses were prepared from commercially available single element 1000 ppm emission spectroscopy

stock solution standards prepared in 1-2% nitric acid. Net counts were calibrated using a “two-point” calibration system involving a blank and a high standard that was prepared to be slightly more concentrated than the highest concentration sample, thus bracketing the concentration range of the samples. Three to four additional standards, spanning the full concentration range of the samples, were also prepared and run as “unknowns” to confirm linear calibration curves and to monitor reproducibility. Samples were run in duplicate.

3.3 Result and discussion

3.3.1 Electrodeposition

Chitosan dissolves in acidic aqueous solution by addition of a proton to the NH_2 group to form NH_3^+. The process is reversible and on increasing pH higher than 6.3, protonated chitosan deprotonates and precipitates. As reported previously by this group [60] as well as in work by Fernendes, et al. [62], a localized zone of high pH is created near a cathode held at sufficiently negative potential in water, a method utilized in this process to electrochemically deprotonate protonated chitosan and form deposits on the steel substrate. Stainless steel is chosen as an electrode as it is inexpensive, easy to use, and does not corrode at cathodic potentials. The presence of an ultrathin passive layer on the steel enhances initial chitosan film formation and sorption, as shown in our previous work.

During cathodic polarization, reduction of H^+ ions results in formation of H_2 gas, as indicated by hydrogen bubble formation on the steel substrate. This removal of H^+ ions from solution creates a zone of high pH near the substrate where chitosan is deposited. The film thus formed is shown in the SEM micrograph in figure 3.1. Chitosan can be seen to have been deposited in a multilayer structure. The first layer of chitosan is formed on the surface of hydrogen bubbles formed on the electrode (indicated in figure 3.1 as the brightest area due to the most penetration of electrons from the substrate below) with diameter around 100 microns (figure3.1) . With the continuation of electrolysis and further accumulation of hydrogen, the bubbles collapse into each other to form larger bubbles of hydrogen 300-400 microns in diameter, leaving the precipitated chitosan structure behind. An additional layer of chitosan is precipitated on top of the new bubbles formed (the areas with intermediate darkness in figure 3.1). The process continues forming still larger bubbles with diameter 300 μm to 1mm forming the top layer of the precipitated chitosan film. The darkest areas (dark due to the blocking of electrons emitted from the substrate below by chitosan) in the figure are those with the maximum amount of chitosan which could have formed by transport of material along the bubble surface (hence making the top of the bubble progressively thinner until it breaks; the resulting fractures in this layer are clearly visible in the picture).

3.3.2 Chemical characterization

The result of FTIR spectroscopy of the deposited material is summarized in table 3.1. The peaks at 1663 cm^{-1}, 1203 cm^{-1} and 970 cm^{-1} indicate oxidation of some of the nitrogen in chitosan as a result of the electrochemical process. Raman spectra of air-dried chitosan film as well as electrochemically modified chitosan are shown in figure 3.2. The peak at 2920 cm^{-1} from the air-dried sample, most likely results from a combination of asymmetric C-H vibration from CH_2OH and C-O stretching vibration from hydroxyl group. The broad peak at 1634 cm^{-1} is expected to result from a combination of amine N-H deformation and aromatic C=C stretching vibrations. The peak at 1465 cm^{-1} is expected to be from the C-H scissor vibration while the peak at 1384 cm^{-1} is expected to be from the CH_2 wagging. Peaks at 1325 cm^{-1} and 1188 cm^{-1} can be attributed to C-N stretching from amine group. The peak at 1256 cm^{-1} can be attributed to OH deformation vibration of CH_2OH group. The peaks at 1188 cm^{-1} and 820 cm^{-1} are expected to be from symmetrical and asymmetrical C-O-C stretching in cyclic ether while the peaks at 935 cm^{-1} and 468 cm^{-1} are expected from C-O-C bonds between monomer units. The peaks at 628 cm^{-1} and 560 cm^{-1} can be attributed to ring vibrations. Raman spectrum of electrochemically deposited material showed various new peaks: a peak at 3345 cm^{-1} from the N-H stretching vibration in C=N-H groups while the peak at 1860 cm^{-1} is expected to be from the C=O stretching vibration. The peak at 1589 cm^{-1} can be attributed to N-H bending in amine and the peak

at 1525 cm^{-1} is consistent with the asymmetric NO_2 stretching vibration. The peak at 901 cm^{-1} is consistent with the C-N stretching vibration in nitro groups, and the new peak at 491 cm^{-1} is expected to be from the NO_2 rocking vibration. Vibrational spectroscopy also indicates oxidation of a fraction of amine to imine and nitro groups as well as oxidation of some of the hydroxyl groups to aromatic ketone.

To confirm oxidation, XPS of the underside of a removed film layer (as described previously) was carried out. The resulting XPS spectrum of electrodeposited chitosan is shown in figure 3.3. Two peaks are present for N1s; with charge correction, they correspond to binding energies of 398.6 eV (NH_2) and a large, broad peak at 407 eV. The peak at 407eV confirms oxidation of nitrogen in chitosan, falling in the range of nitrate in cellulose nitrate (408.1eV) and C-NO_2 nitro compounds (406.3 eV)[63].

Hence, vibrational and X-Ray spectroscopy provide clear evidence oxidation of at least a portion of the amine groups in chitosan to nitro groups and some hydroxyl groups to aromatic ketone. The estimated structure of this novel molecule is shown in figure 3.4. The oxidation is expected to have taken place by reaction of amine and hydroxyl group with OH^- Ions formed by electrolysis of entrapped water molecules in the hydrogel structure as shown in equations below.

$-NH_2 + OH^- \rightarrow =NH + H_2O + e^-$ equation (1)

$=NH + 5OH^- \rightarrow =NO_2 + 3H_2O + 5e^-$ equation (2)

$$-OH + OH^- \rightarrow =O + H_2O + e^- \qquad \text{equation (3)}$$

Exposure of hydrogel to ultraviolet light was found to increase the intensity of the oxidized nitrogen peak in X-ray photoelectron spectroscopic spectrum (not shown) indicating oxidation of higher fraction of amine. Enhanced oxidation of nitrogen by hydroxyl ion in presence of UV light has also been observed by other researchers [64].

3.3.3. Equilibrium adsorption isotherms

The amount of metal adsorbed per unit mass of electrochemically modified (ECM)-chitosan, Q_e, was calculated using formula:

$$Q_e = \frac{(C_i - C_e)V}{M} \qquad \text{equation (4)}$$

Where C_i is the initial concentration and C_e is equilibrium concentration in mg/l and M is dry mass of adsorbent in mg. The results of batch equilibrium adsorption are shown in figure 3.5. The amount of chromium adsorbed by unit mass of ECM-chitosan increases with initial concentration of chromium till a plateau was achieved at 300ppm, a result was similar to observations involving other forms of modified chitosan.using poly(2-acrylamido-2-methypropane sulfonic acid) and poly 3-methyl thiophene [65,66]. The adsorption capacity was found to be 174.4 mg Cr(VI)/g of ECM-chitosan which is higher than values observed for modifications of chitosan by Verma at el.[67] and the references cited therein.

Equilibrium adsorption isotherms were used to investigate interactive behavior between the solution and adsorbent. A widely used Langmuir model which is representative of monolayer adsorption occurring on an energetically uniform surface without interactive molecules [68], was found to fit the process successfully(figure 3.6). The Langmuir model (equation 5) and its linear transformation(equation 6) are given below.

$$Q_e = \frac{Q_m B C_e}{1 + BC_e} \qquad \text{equation (5)}$$

$$\frac{1}{Q_e} = \frac{1}{Q_m} + \frac{1}{bQ_m C_e} \qquad \text{equation (6)}$$

Where Q_e is equilibrium adsorption capacity (mg/g), Ce is the solution concentration at equilibrium(mg/l) Q_m is Langmuir constant representing maximum adsorption capacity(mg/g) and b is the Langmuir constant related to energy of adsorption (l/mg). The calculated value of Q_m was 500 mg/g which is well above the experimentally observed value. The calculated value of b was 0.001 l/mg, with a correlation coefficient (R^2) of 0.9909. A dimensionless separation factor (R_L) was used to determine efficiency of adsorption obtained by equation $R_L = 1/(1+bC_0)$ where C_0 is initial concentration. The positive value calculated for b ensures an R_L value between 0 and 1 indicating the process of adsorption is feasible.

3.3.4 Effect of pH on adsorption of Chromium

The pH of the adsorption medium influences the physicochemical

interactions between dissolved ions and adsorptive sites on the adsorbent [69]. The effect of pH on adsorption of chromium (VI) by electrochemically modified chitosan in the pH range of 1 to 8 is shown is figure 3.7. The maximum adsorption of Cr was observed for pH 3 followed by a plateau region between pH 4-7, while the adsorption capacity of ECM-Chitosan was found to collapse on reaching pH8. Chromium exists as H_2CrO_4 at pH less than 2 which accounts for the low value of adsorption at very low pH. The precipitation of chromium due to presence of OH^- ions can be a contributing factor towards the near complete lack of adsorption at pH higher than 8.

The adsorption behavior at intermediate pH values can be due to several single or combined effects. Adsorption most likely occurs due to formation of a pendant structure with nitro and oxidized hydroxyl groups. At low pH the surface of the ECM chitosan, just like pure chitosan, would be surrounded by hydronium ions which would increase attractive force between chromium(VI) and binding sites [70].Upon increasing pH, fewer hydronium would be present thus reducing this attractive force. Adsorption may also occur due to electrostatic attraction between any remaining positively charged amino groups and negatively charged chromate/dichromate ions in solution [71], a process which would be enhanced with reconversion of nitro groups to amino groups at very acidic pH values.

3.3.5 Sorption kinetics

Chromium removal by ECM-chitosan as a function of contact time is shown in figure 3.7. The reaction was rapid initially with 50% metal uptake complete within first 5 minutes after which it proceeded slowly and equilibrium was achieved in 3 hours. To further investigate adsorption, mechanism and rate controlling step kinetic models were used. Pseudo first order, pseudo second order as well as inter particle diffusion models were used for analysis. The pseudo second order reaction (equation 7) was found to fit the experimental data successfully (figure 3.8).

$$\frac{t}{q_t} = \frac{1}{kq_e^2} + \frac{1}{q_e}t \qquad \text{equation (7)}$$

The value of k was found to be 2.038 g/mgh with a linear correlation coefficient of 0.9987 indicating that the rate controlling step in chromium adsorption is chemisorption involving valence forces through the sharing or exchange of electrons between chromium and ECM-chitosan [72] in the concentration range tested.

3.3.6 Chloro-chitosan

During application of high negative potentials on working electrode for chitosan deposition a side phenomenon was observed at counter electrode. It was found that chlorine from HCl used to adjust pH of chitosan was being oxidized at anode. Nascent chlorine is extremely reactive and readily reacted with chitosan in the vicinity of electrode

forming a white product. While in concentrated solution the new polymer formed was found to be deposited on platinum electrode, in dilute solution it was found to possess frothy disposition. The froth was skimmed, dried, rinsed and analyzed using Raman spectroscopy.

Figure 3.9 shows the spectrum of the polymer formed at counter electrode. The presence of peak at 3347 cm^{-1} attributed to amine N-H stretching vibration indicates the amine group was intact after reaction of chitosan with chlorine. Other peaks typically present in chitosan at 2889 cm^{-1}, 1658 cm^{-1}, 1379 cm^{-1}, 1119 cm^{-1} and 933 cm^{-1} assigned to C-H stretching, C=C stretching, C-H_2 deformation, symmetric C-O-C stretching vibration and ring vibration respectively. In addition a new peak at 737 cm^{-1} associated with C-Cl was observed, the result shows that chlorine reacts with chitosan in solution and displaces one or both of hydroxyl group from the chain. Estimated structure of the polymer is shown in figure 3.10.

Peak (cm^{-1})	Assignment
1663	combination of amide I C=O stretching, asymmetric NO_2 stretching and OH deformation vibrations
1585	NH bending frequency
1442	C-C stretching vibration
1380	combination of CH_3 deformation and CO stretching frequencies
1203	combination of NH deformation and symmetric NO_2 stretching vibrations
1154, 1020	symmetric and asymmetric stretching vibrations of C-O-C respectively
970	amine oxide
805	O-H deformation

Table 3.1: Peak positions and assignments for Fourier Transform Infrared spectrum of electrochemically modified (ECM) chitosan.

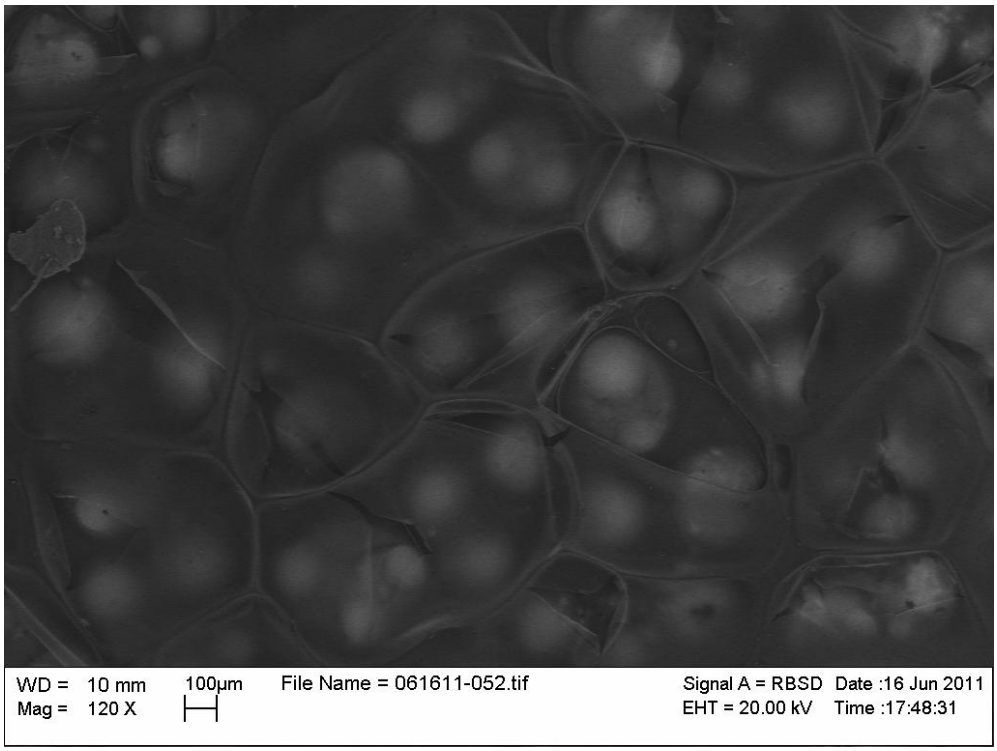

Figure 3.1 : Scanning electron microscopy of electrochemically deposited chitosan on stainless steel at -3.0V vs Ag/AgCl reference electrode.

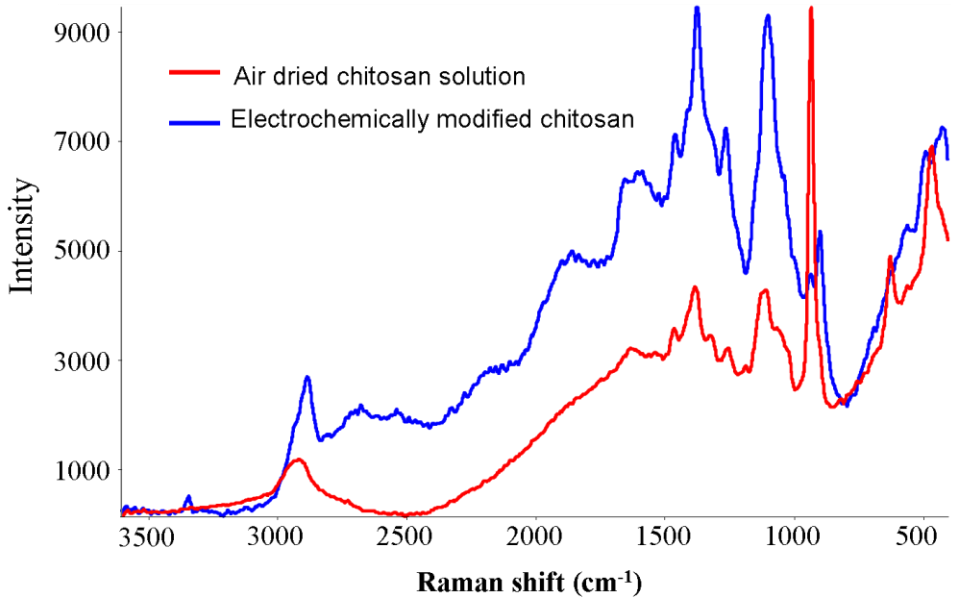

Figure 3.1 : Raman spectra of ECM-chitosan and dried chitosan solution at pH2.

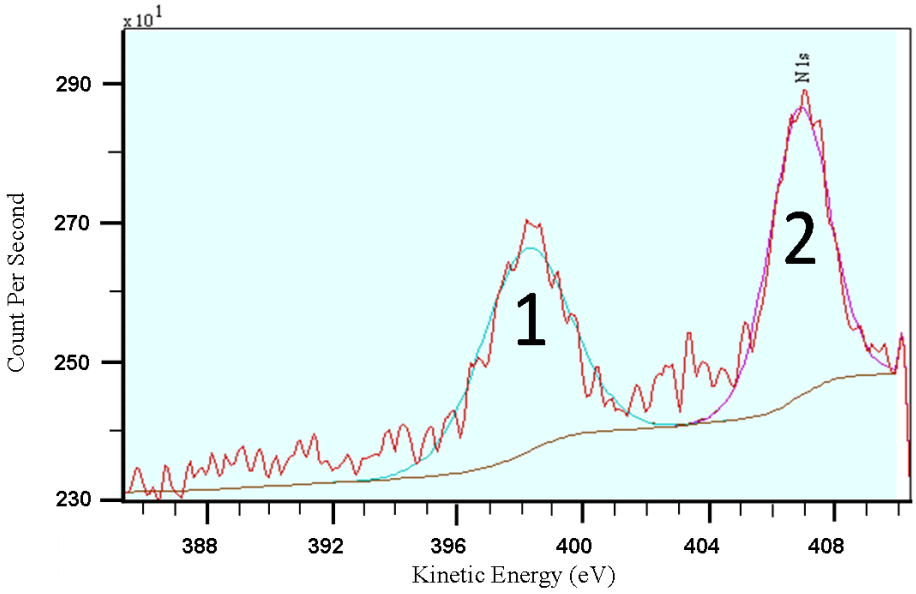

Figure 3.2 : XPS of electrodeposited chitosan . Peak 1: primarily amine (-NH2), Peak 2: similar to nitrate, possible nitronyl (N=O).

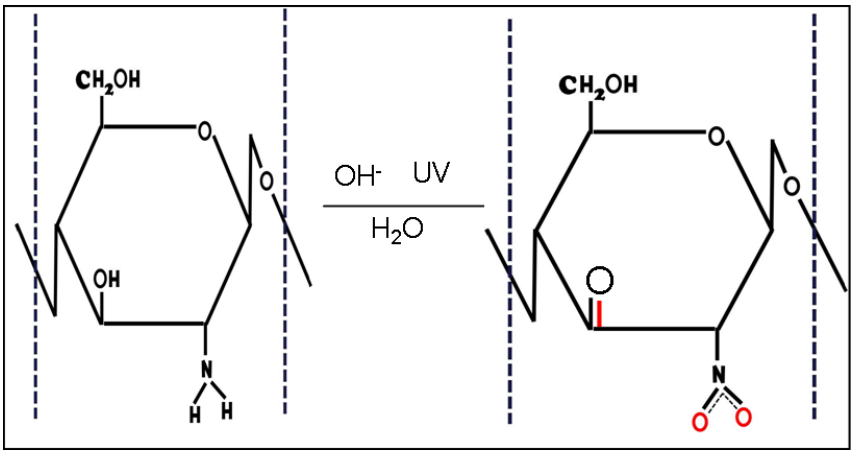

Figure 3.3 : structures of chitosan and nitro-chitosan synthesized by electrochemical deposition and photochemical oxidation.

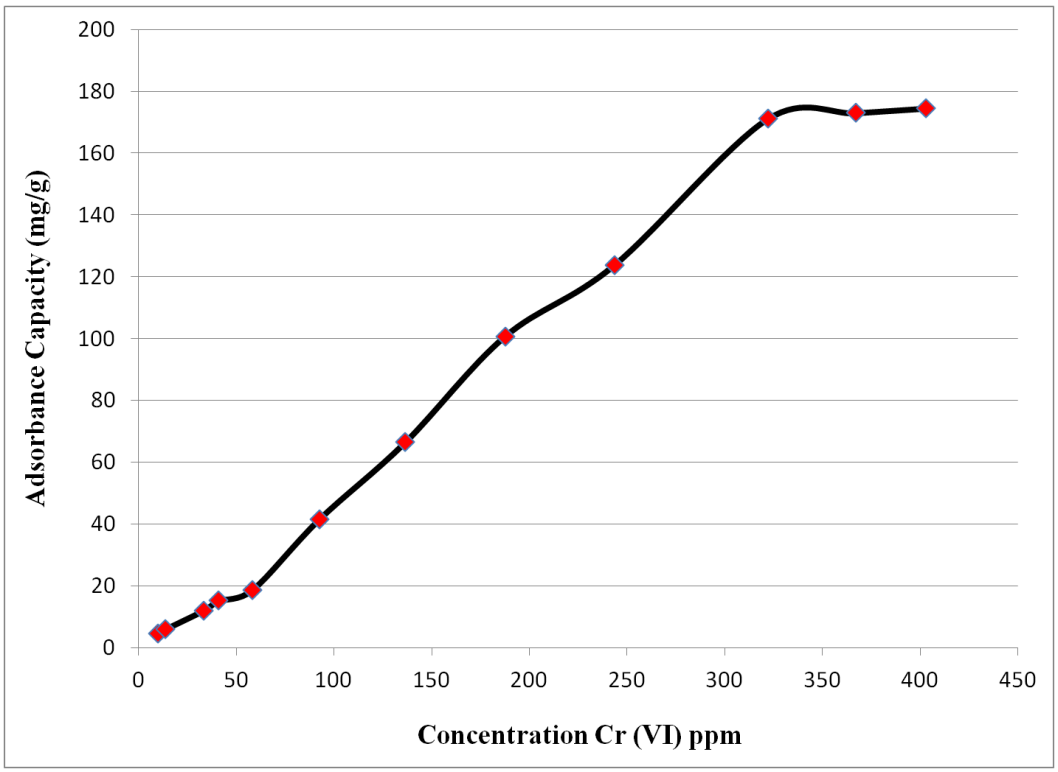

Figure 3.4 : Isotherm for adsorption of Cr(VI) onto ECM-chitosan

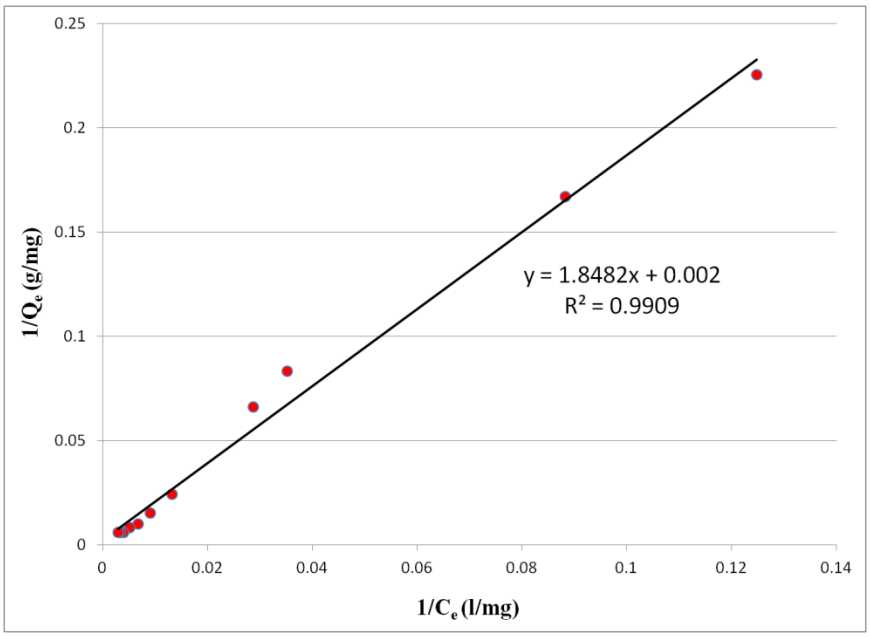

Figure 3.5: Langmuir plot for adsorption of Cr(VI) onto ECM-chitosan.

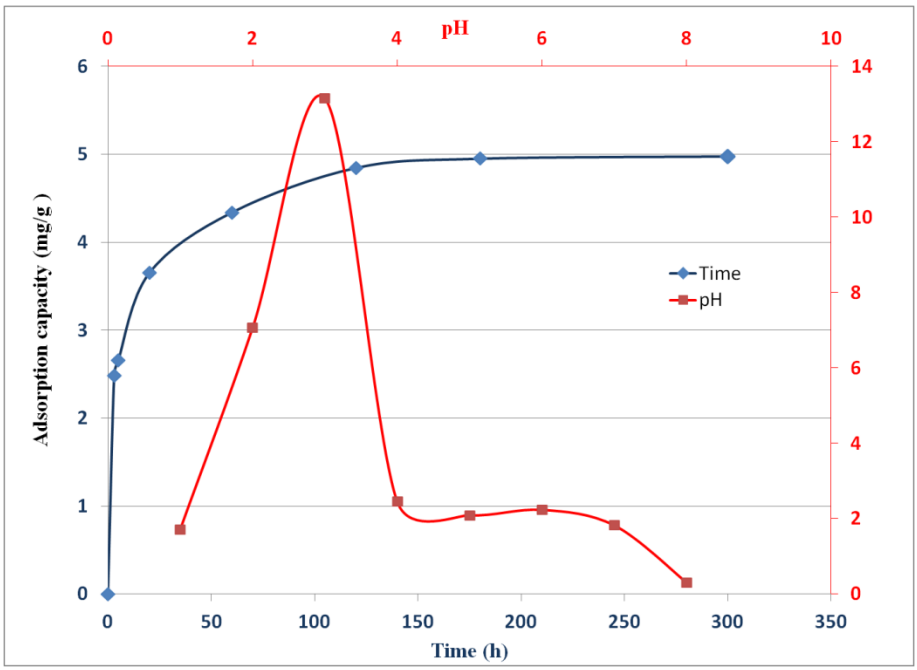

Figure 3.6: Effect of pH (red) and contact time (Blue) on chromium adsorption onto ECM-chitosan.

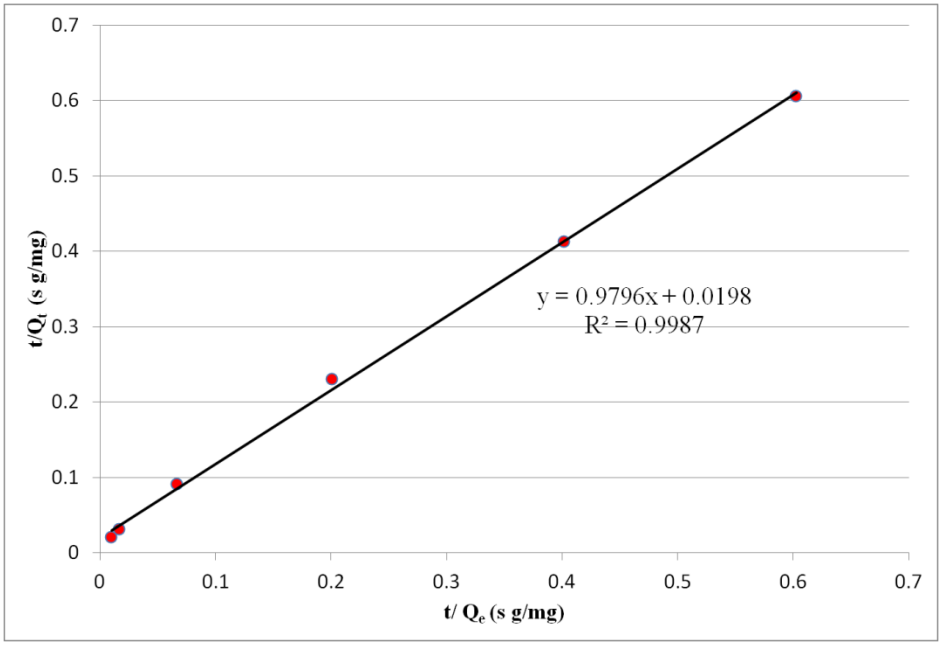

Figure 3.7: Curve fitting by pseudo second order reaction model on adsorption.

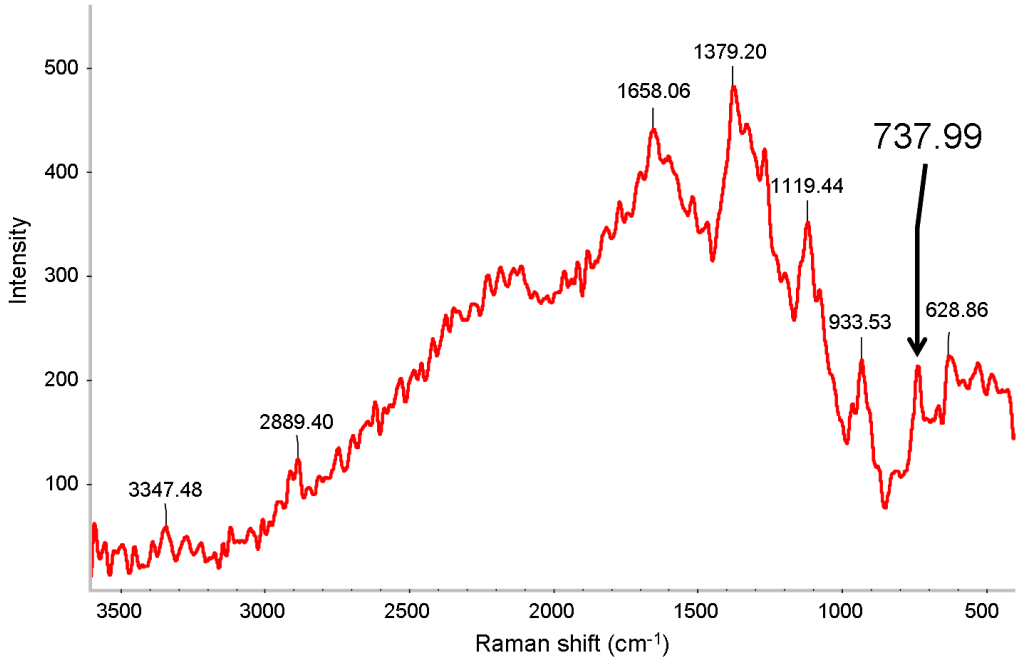

Figure 3.8: Raman spectrum of polymer formed on counter electrode at -2.0V versus Ag/AgCl, showing C-Cl vibrational peak.

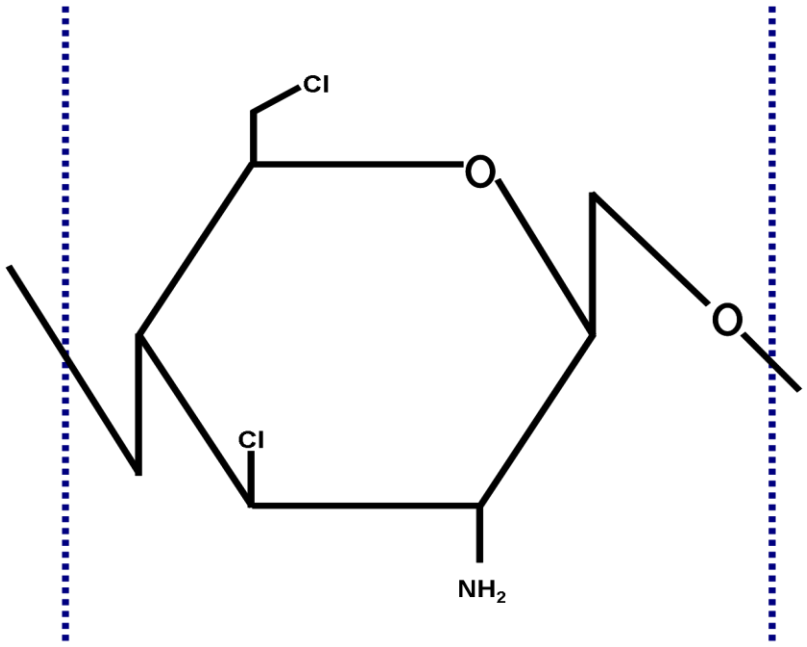

Figure 3.9: Expected structure of chloro-chitosan.

Chapter 4 : Polysaccharide assisted electrochemical pathway for formation of silver and palladium nanoparticles for catalytic applications.

4.1 Introduction

Inexpensive, “green” materials for catalytic applications in energy, environmental and biomedical engineering are required for innovation in device development and manufacturing. [73] In the area of fuel cell development, catalytic electrode surfaces for key chemical reactions, including the hydrogen evolution reaction (HER) and oxygen reduction reaction (ORR) are required which are durable, inexpensive and easy to manufacture [74]. Environmentally-benign manufacturing techniques which eliminate harsh or toxic chemicals and which can proceed at low pressure, room temperature and in simple operating environments, are especially valuable[75] This is especially true if the methods used are adaptable, both in terms of materials used and geometry of the device produced. Tolerance of variability in source materials is critical, as manufacturability and quality depend on the ability to meet performance criteria in a robust fashion. Conformal coatings, for example, provide the ability to be adapted to multiple surface geometries and sizes [76].

While PEM fuel cells are receiving much of the attention in commercial research and development, alkaline fuel cells (AFC) have a long history of use by NASA for power requirements of satellites, and are

being further explored by a number of companies due to certain advantages including an electrical efficiency of 50% or more. In general, the possibility of using less expensive materials made possible by lower overpotential requirement make AFC a commercially attractive technology [77].

Metal nanoparticles have been identified as an extremely important class of catalysts for a variety of chemical processing needs, including for the conversion of organic compounds in energy generation[78], use in polymer membranes in hydrogen fuel cells, chemical synthesis (e.g. carbon-carbon bond formation and oxidation reactions[79]) and a number of other reactions. Silver have been identified as catalyst for oxygen reduction reaction (ORR)[81] in AFCs, the works on silver nanoparticles for ORR include; controlling size of nanoparticles using DMSA by Lu and Chen[82], bimetal catalysts using platinum[83, 84, 85], palladium [86, 87,88] and cobalt [89,90]. Most reported fabrications of catalytic metal nanoparticles (e.g. Ag, Au, Pt and Pd) involve a three stage process requiring: (a) a metal salt in solution; (b) a “shaping” or encapsulation agent, which is usually an organic molecule, [80]; and (c) a strong reducing agent (e.g.$NaBH_4$) to reduce the metal ions for the formation of nanoparticles. It is this third highly reactive component which is often an environmental or health hazard, and which limits the sustainability of the chemical process.

Chitosan, a linear polysaccharide of 2-amino-2-deoxy-D-

glucopyranose obtained by deacetylation of chitin from crustaceans, mollusks, insects and fungi, is the second most abundant natural biopolymer (after cellulose). It has found a broad range of applications in the form of powder, flakes, beads, and occasionally fibers and membranes in the pharmaceutical, food processing and medical industries due to its biocompatibility and non-toxicity, its excellent gel and film-forming ability [56]. In present work we report a novel two step electrochemical process for nanoparticles fabrication using chitosan. Silver nanoparticles were grown by electrochemical reduction of Ag^+ on a chitosan film. Particle size was controlled by optimizing voltage time and thickness of chitosan film. The synthesized nanoparticles were tested for catalytic activity and were found to be a good candidate for the ORR for fuel cell and other applications.

4.2 Experimental

4.2.1 Materials

Chitosan solution was prepared by dissolving 1.5g of low molecular weight chitosan (obtained from Aldrich) in 120 ml of deionized water (>18mΩ/cm). Silver nitrate(>99% purity) was obtained from Sigma-Aldrich, 0.1M solution was used for silver deposition. 304 stainless steel sheet 12”X12” 0.036” thickness with #8 mirror finish was obtained from McMaster-carr. All other chemicals used were reagent grade.

4.2.2 Scanning Electron Microscopy

The SEM system used was a Leo 1550 with a Robinson back scatter Gemini detector with EDAX, BS, AC, EBSP, SE, InLens detectors. Back scattered images were used to investigate morphology of Silver particles deposited and EDS pattern was used to estimate chemical composition of particles formed.

4.2.3 UV-Vis spectroscopy

UV-Vis measurements were taken using an USB4000 spectrometer with Analytical Instrument Systems Inc. Model DT 1000 CE UV/VIS light source and data was collected in 250-900 nm wavelength range. Data accumulation and processing were performed using Spectra Suite software.

4.2.4 Synchrotron FTIR

Fourier Transformed Infra Red spectroscopy were conducted at beamline U10B at Brookhaven National Laboratory using a Hyperion 3000 IR microscope in 900-4000 cm^{-1} frequency range with a resolution of 4.0cm^{-1}. Data accumulation and processing were done with OMNIC for Nicolet Almega version 7.3.

4.2.5 Cyclic Voltammetery

Cyclic Voltammetry measurements to monitor oxygen reduction

reaction were done using Gamery reference 600 potentiostat and data acquisition was done using Gamry Echem software. The measurements were performed using a three electrode assembly with 1mV resolution. While silver/chitosan nanocomposite on stainless steel was used as working electrode, platinum wire served as the counter electrode and Ag/AgCl was used as the reference electrode. All measurements were done at 20mV/s scan speed. A custom designed electrochemical cell was used and the electrolyte(0.1M NaOH) was purged with oxygen(>99.6% pure) for ORR and with nitrogen (>99.99 pure) for comparison.

4.2.6 Silver-Chitosan Composite synthesis

An electrochemical layer of chitosan was deposited on stainless steel the method for electrochemically-induced deposition is based upon cathodic polarization of the electrode on which deposition is to occur – a process which has long been shown to create a region of higher pH (> 6.3, due to hydrogen evolution) [91]. The process of chitosan deposition on stainless steel has been reported in our earlier work [60]. Chitosan was deposited for 120 seconds at a potential of -2V Vs Ag/AgCl. The hydrogel thus formed was rinsed with DI water to remove any HCl still present; the film was then left to dehydrate for 24 hrs. Silver deposition on chitosan coated stainless steel was carried out by applying negative potential to the electrode in a 0.1M silver nitrate solution. Silver deposition on the composite electrode was conducted at varying time as well as voltage to access the effects of parameter variables on size and morphology of

nanoparticles deposited.

4.3 Results and discussion

4.3.1 Silver deposition

Silver was found to be successfully deposited on chitosan at reducing potentials; the structure formed at -0.5V after 60 seconds of deposition is shown in figure 4.1. The deposition was found to occur in three different stages depending on thickness of chitosan film initially formed. The initial chitosan layer is formed on the steel surface on the surface of small hydrogen bubbles created through cathodic reduction of protons at the solution interface. The craters formed by collapse of the smallest bubbles are ~100 μm in diameter and have the thinnest layer of chitosan; silver deposition initiates at these sites. After 60 seconds of deposition at -0.5V the particles showed dendritic growth forming structures up to 20 μm long. Additional nuclei on which growth has not yet taken place can also be seen in this area in the figure. In the areas of intermediate thickness (where bubbles 300-400 μm diameter formed) nucleation with 40-100 nm long nuclei was found but no growth was observed. The areas with thickest layer of chitosan showed no presence of silver for this voltage and deposition time, consequently these areas were darkest in the image.

The schematic is shown in figure 4.2. At stage (a) hydrogen bubbles are formed on steel electrode in chitosan solution creating a localized zone of high pH caused by removal of H^+ ions form the solution. 2(b)

shows the stage when protonated chitosan is depronoted and deposited over bubbles and in areas between them. 2(c) depicts the stage where the bubbles formed at stage (a) collapse into each other leaving thin film of chitosan behind. A new layer of chitosan is formed on top of bigger bubbles formed. The process gets repeated thus forming “circular step” structure with thinnest layer of chitosan at sites of initial bubble sites and so on. It is at these sites that nucleation of nanoparticles takes place as shown in figure 4.2(d).

4.3.2 Effects of deposition time on Ag nanoparticles

The effect of deposition time on size and distribution of silver nanoparticles on chitosan was analyzed by depositing silver at -3V vs. Ag/AgCl for different time periods; the results are shown in figure 4.3. It was observed that after five seconds there were multiple nucleation sites and a very few particles which grew to a size of 1 µm. After ten seconds of deposition no significant increase in number of nucleation sites was observed; however, the bigger particles continued growing and at this stage dendritic structures could be seen. The largest particles at this stage were several microns in length. After fifteen seconds of deposition significant growth was observed at multiple locations, and cubical particles of silver were found to have grown on top of dendrites. The cubes formed were 200-500nm wide while the dendrites below them were about 10 µm long. Further growth was observed and by thirty seconds aggregated of

particles 20-30 μm in size could be seen. At this stage, both the dendrites as well as cubes were found to be covered with nanoparticles 10-20 nm long.

The results at fixed voltage indicate that reduction of silver through the chitosan layer has two rate controlling steps. Initially the rate of growth of particles depends upon conduction through the chitosan layer as evident from nucleation at the thinnest regions of the film and the initial growth of dendrites. After this initial growth stage, a large surface area of silver is available for reduction of Ag^+ ions and the rate is limited by amount of Ag^+ ions in solution as evidenced by formation of smaller nanoparticles on top of structures already formed at thirty seconds.

4.3.3 Effects of deposition Voltage on Ag nanoparticles

In the next set of samples the time of deposition was kept constant at sixty seconds and voltages chosen were -2.0V, -1.5V,-1.0V and -0.5V. While all the samples showed dendritic structure (not shown) in the thinnest region of the chitosan layer, significant differences were observed in the vicinity of dendrites as shown in figure 4.4.

At -2V and -1.5V a flat islanded structure was found to have been formed. While at -2V the islands were found to have grown into one another, at -1.5V open areas between islands could be seen indicating that islands are formed by growth of nanoparticles in X and Y direction.

Thickness of the chitosan layer does play a role in island formation as these were primarily found in the areas with an intermediate thickness of chitosan; understanding the exact nature of growth of islands requires further exploration. No island formation was observed from deposition at -1V and -0.5V. Some cubic crystals were formed on dendrites at -1V, but at -0.5V only dendrites and nanoparticles were found to be present. Based on time and voltage optimization, operating parameters for silver deposition for the remainder of the experiments were chosen to be -0.5V for 30 seconds. A second layer of chitosan deposition was formed on top of the initial deposited layer to improve homogeneity of the surface structure for further experiments; the resultant structure with improved homogeneity of distribution and uniformity in thickness is shown in figure 4.5.

4.3.4 Spectroscopic analysis of Ag-chitosan composite

UV-Vis spectroscopy of sliver NPs on chitosan showed broad bands due to surface plasmon resonance (SPR) at λ_{max} ~460nm and ~350nm (figure 4.6). The band at 350nm is attributed to multipole transitions of surface plasmon [92]. The band at 460nm is red shifted from SPR of pure silver at around 420nm [93], the shift is expected to be caused by presence of nanoparticles of varying shapes and thus varying absorption maximum [92]. The sharp decline in intensity of peak at right hand side is expected to be caused by limit on maximum size of nanoparticles, as

broadness of band is caused by broad size distribution [93].

Synchrotron IR spectroscopy (figure 4.7) of pure chitosan when compared to that of an Ag nanoparticle/chitosan composite layer shows several distinct differences, including the loss of a shoulder at 3440 wavenumbers and the replacement of the doublet at 1660/1590 wavenumbers by a single dominant peak at 1600, both indicative of complexation at the amine group of chitosan. Additional changes occur in the peaks at 1300-1450 wavenumbers (the amide II region) indicating additional complexation. What is not clear is whether amine groups oxidize during the deposition process (due to electrochemical polarization), and this in turn leads to subsequent association with silver nanoparticles formed , or whether bonding occurs on exposure of chitosan film to Ag^{+} solution prior to application of voltage and reduction of the silver ions. It is also possible that individual Ag ions may be complexed with chitosan while the metallic nanoparticles are separately associated with the chitosan matrix through liganding.

4.3.5 Oxygen reduction reaction on Ag nanoparticles

Figure 4.8 shows cyclic voltammetry data obtained on the nanoparticles in oxygen saturated 0.1M NaOH. CV for AgNP showed reduction peaks at 0.23V, -0.5V and -0.86V. The peak at 0.23V can be attributed to oxygen reduction by a 4 electron reduction pathway as shown in equation 1. The small peak at -0.5V is associated with the 2 electron

pathway of oxygen reduction (equation 2) [96]. The peak at -0.86V is expected to be oxygen reduction by single electron transfer as shown in equation 4 [97] and not the two electron pathway shown in equation 3, as evident from the presence of cathodic peak at -0.45V which is associated with oxidation of superoxide radical anion (O_2^-). Shifting of the reduction peak to more negative and oxidation peak to more positive potentials can be due to potential barrier resulting from complexation of Ag with chitosan, similar to iodine adlayer on gold as observed by Miah and Ohsaka [96].

$O_2 + 2H_2O + 4e^-$ → $4OH^-$ Equation (8)

$O_2 + H_2O + 2e^-$ → $HO_2^- + OH^-$ Equation (9)

$HO_2^- + H_2O + 2e^-$ → $3OH^-$ Equation (10)

$O_2 + e^-$ ⇔ O_2^- Equation (11)

Ag ⇔ $Ag^+ + e^-$ Equation (12)

Silver oxidation and reduction peaks as shown in equation 5 were also observed: oxidation of silver nanoparticles started at 0.44V and peaked at 0.55V and reduction of Ag^+ was observed in a broad range with the peak centered at 0.56V. The onset of oxidation of silver was observed to occur at a 200 mV higher positive potentials than that observed by Guo et. al. [95] The stability of nanoparticles formed is expected to be a result of complex formation with the amine group of chitosan. The difference of 190mV between silver oxidation and oxygen reduction through the 4

electron pathway makes electrochemically synthesized silver nanoparticles onchitosan an excellent candidate for catalysis in alkaline fuel cells.

4.3.6 Formation of palladium nanoparticles

Even though the reduction potential of Pd^{2+} (-0.987V v/s NHE) is similar to that of Ag^{+} (-0.799V v/s NHE) the two step processing of nanoparticles could not be applied to palladium. The reason for the phenomenon can be reaction of palladium with chloride ions present in the solution resulting in the formation of PdCl42^{-}. $PdCl_4^{2-}$ has a reduction potential of -1.8V, thus electrolysis of water also takes place at the voltage required. The vigorous evolution of gaseous hydrogen at the steel-chitosan interface is detrimental for the chitosan film in palladium nitrate solution, and the film was found to have lost adhesion with the steel at this highly negative potential.

One step deposition was thus employed for palladium nanoparticle synthesis. Varying amounts (10, 25, 50 % v/v) of 0.01M palladium nitrate solution was added to chitosan stock solution. A potential of -2.0V (vs Ag/AgCl) was then applied to the steel working electrode to co-deposit chitosan and palladium. A schematic of the process is shown in figure 4.9. It was found that palladium was still not electrochemically reduced, but rather formation of Pd metallic nanoparticles occurred by reduction of Pd with hydrogen with two distinct morphologies.

Figure 4.9(a) shows formation of first morphology: palladium is reduced over hydrogen bubbles while hydrogen is still being formed. This process leads to pressure build up inside the bubble which eventually ruptures leaving behind the structure formed as shown in figure 4.9(b). The morphology created by this mechanism is shown in figure 4.10.

The second morphology involves formation of fine Pd nanopartcles suspended in solution. After rupture of the bubble, escaping hydrogen reacts with Pd^{2+} ions in solution creating very fine particles (the size of the particles were too small to be estimated using SEM at 100K magnification). Some of these particles get deposited over the film formed (figure 4.11) while most particles remain in solution turning it black from reddish brown. The solution was filtered with a Sarstedt Teflon filter (pore size 0.45µm). Even though some of palladium passed through the pores the filter was found to be fully clogged after filtration of less than 5ml solution. Strong association of palladium with chitosan is expected to be responsible of pseudo large size of nanoparticles. . X-ray diffraction of the particles attached to the Teflon filter show the presence of nanocrystalline metallic palladium formed (figure 4.12), Chitosan peak at $2\theta = 22^{o}$ can also be clearly seen suggesting association between chitosan and palladium.

Further spectroscopic analysis of the Pd nanoparticles will be needed to identify the nature of the association of chitosan functional groups with the metal surface. Studies will also be required to better understand the

durability and functionality of the particles for catalytic applications.

4.4 Conclusions

Silver nanoparticles with controllable size can be efficiently grown on electrochemically deposited chitosan. The initial chitosan layer has sufficient conductivity to facilitate reduction of Ag^+ and conduct charge from steel to silver for the ORR, though the exact nature of conductivity needs further exploration. Through the use of electrochemical formulation of chitosan-based metal-composites, we reduce the need for enzymes and chemical processing steps involving non-renewable solvents (resulting in a more sustainable process). By depositing electrochemically, we also gain the added benefit of being able to incorporate reduction of metal ions into the process for design and development of composites and the “green” manufacture of nanoparticles. Our process uses a room temperature, rapid technique taking advantage of electrochemical reduction to develop a nanoparticle/chitosan layer composite. Our method not only incorporates the principles of “green” chemistry but also is an important step toward design of a sustainable manufacturing technology for metal nanoparticle composites that is rapid, safe and inexpensive.

In contrast to the formation of Ag nanoparticles through electrochemical reduction, Pd nanoparticles were apparently formed through reduction by hydrogen (generated through a hydrogen evolution

reaction on the cathode) but were found to be attached to chitosan film. Catalytic activity of palladium over chitosan film for electrodes needs to be tested especially after the fact that conductivity of films have been observed.

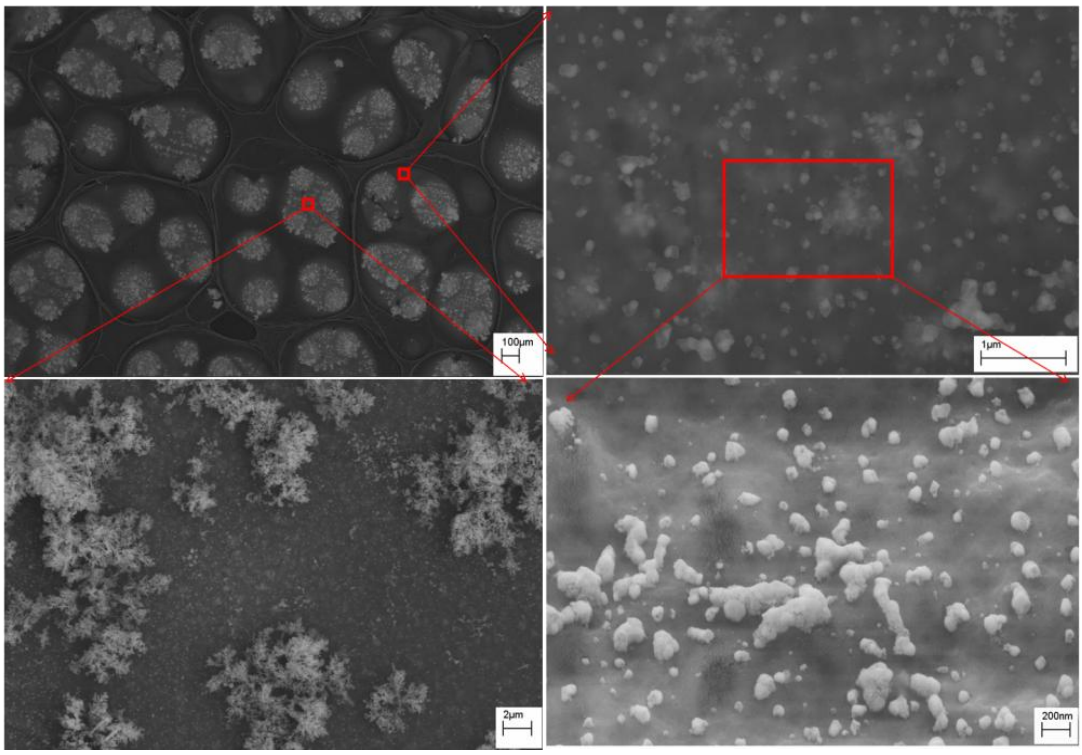

Figure 4.1: Scanning electron microscopic image of Ag deposited on chitosan at -0.5V for 60 seconds shown at different magnifications.

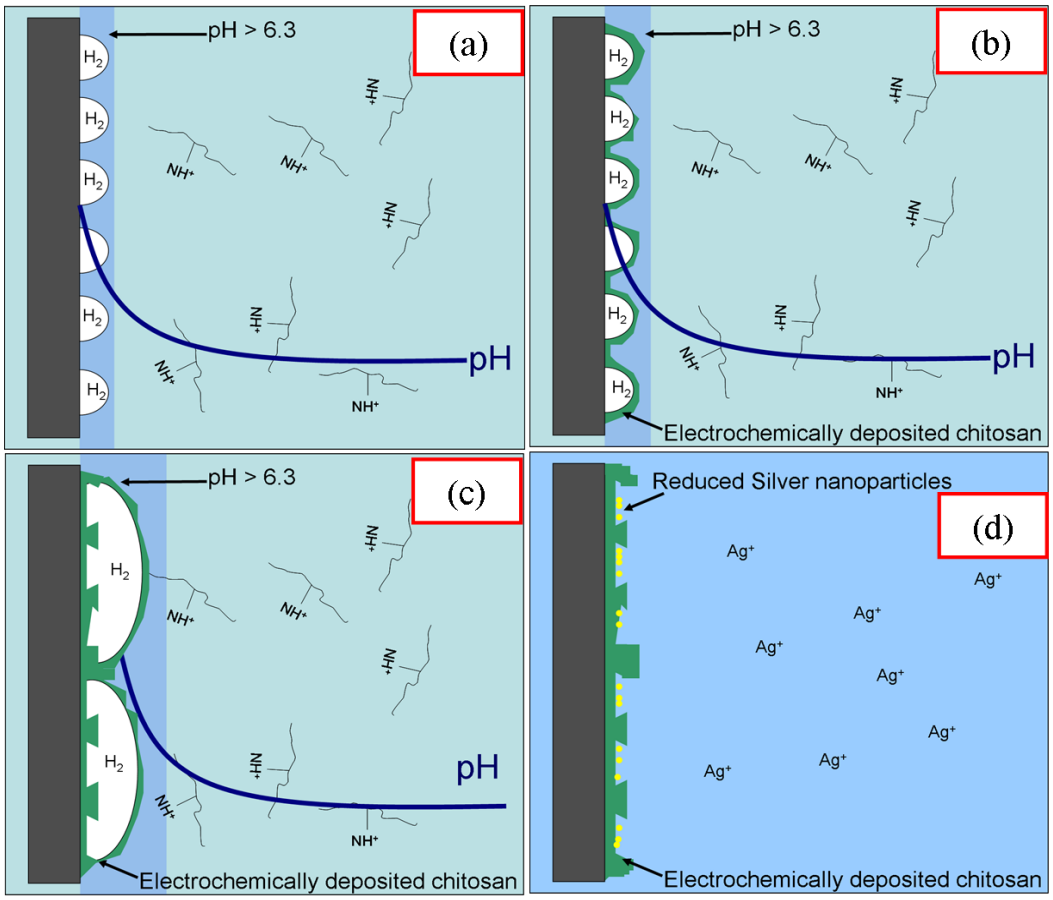

Figure 4.2: Schematic diagram of silver nanoparticles formation.

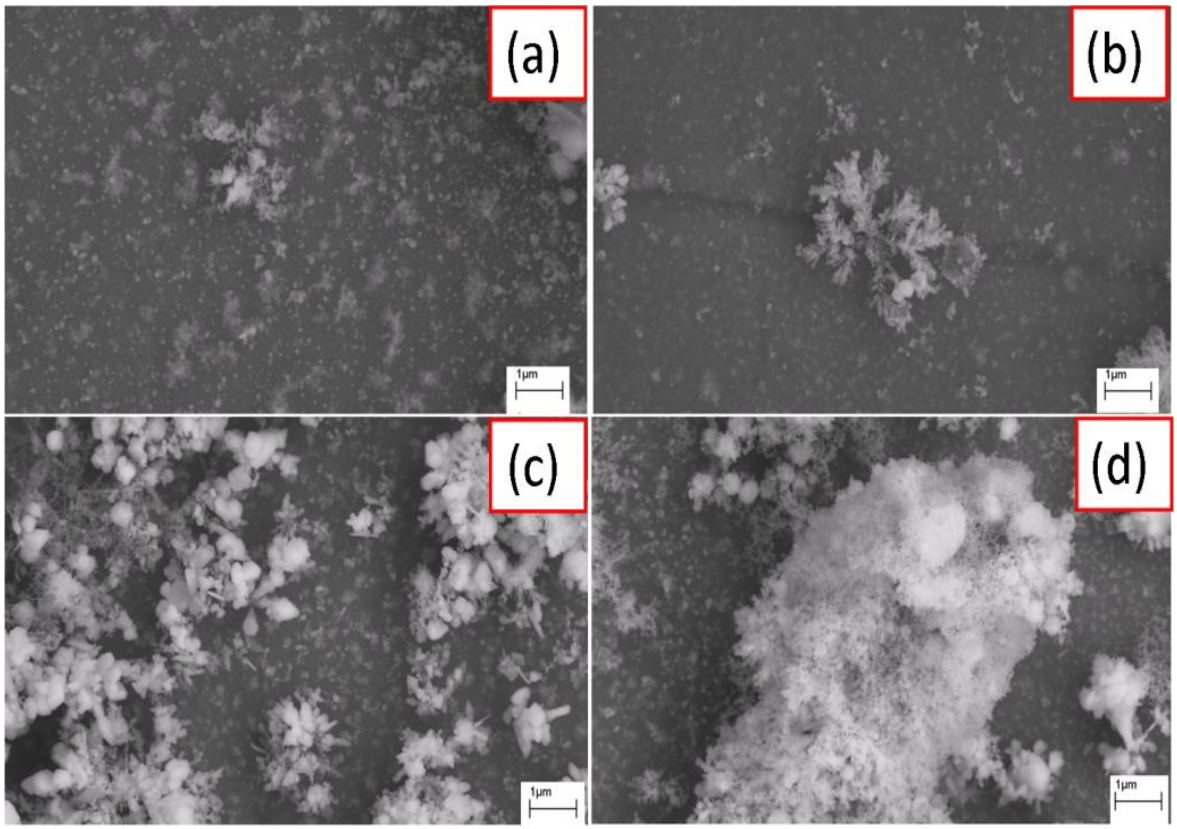

Figure 4.3: Scanning electron microscopic image of Ag deposited on chitosan at -3.0V for 5(a), 10(b), 15(c) and 30(d) seconds.

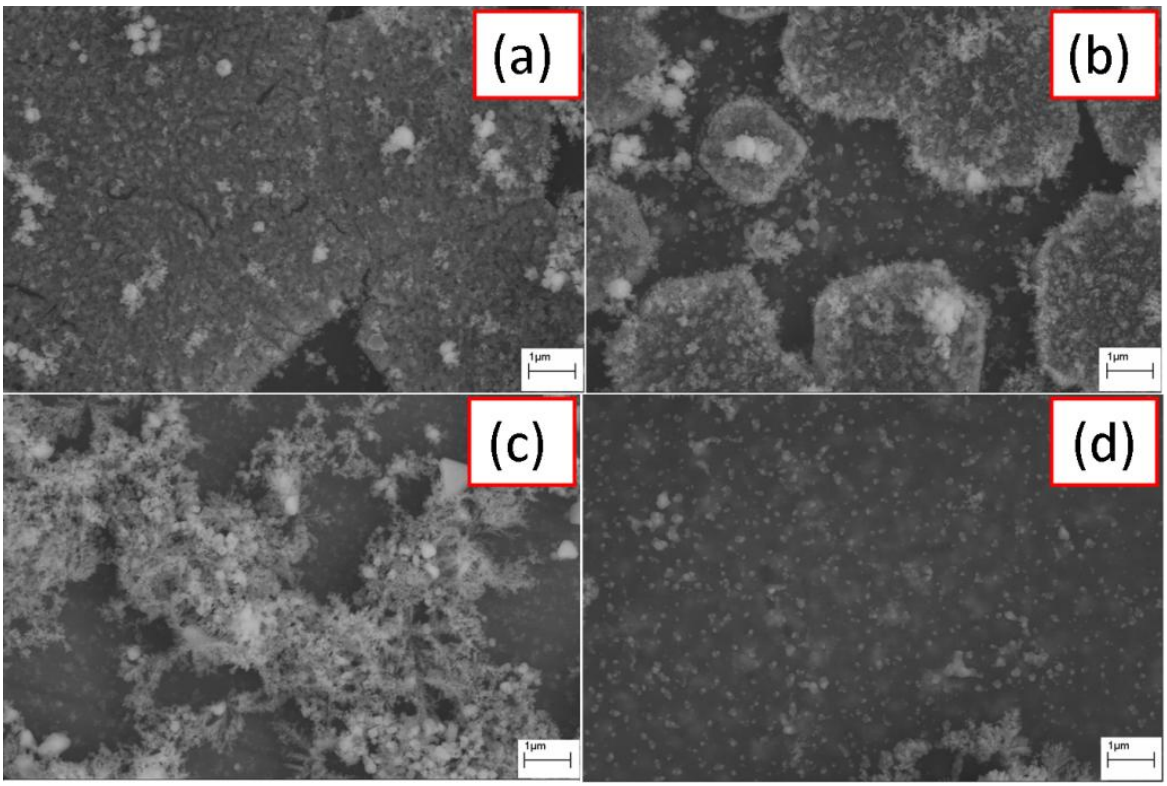

Figure 4.4: Scanning electron microscopic image of Ag deposited on chitosan at for 60 seconds at -2.0V(a), -1.5V(b), -1.0V(c) and -0.5V(d).

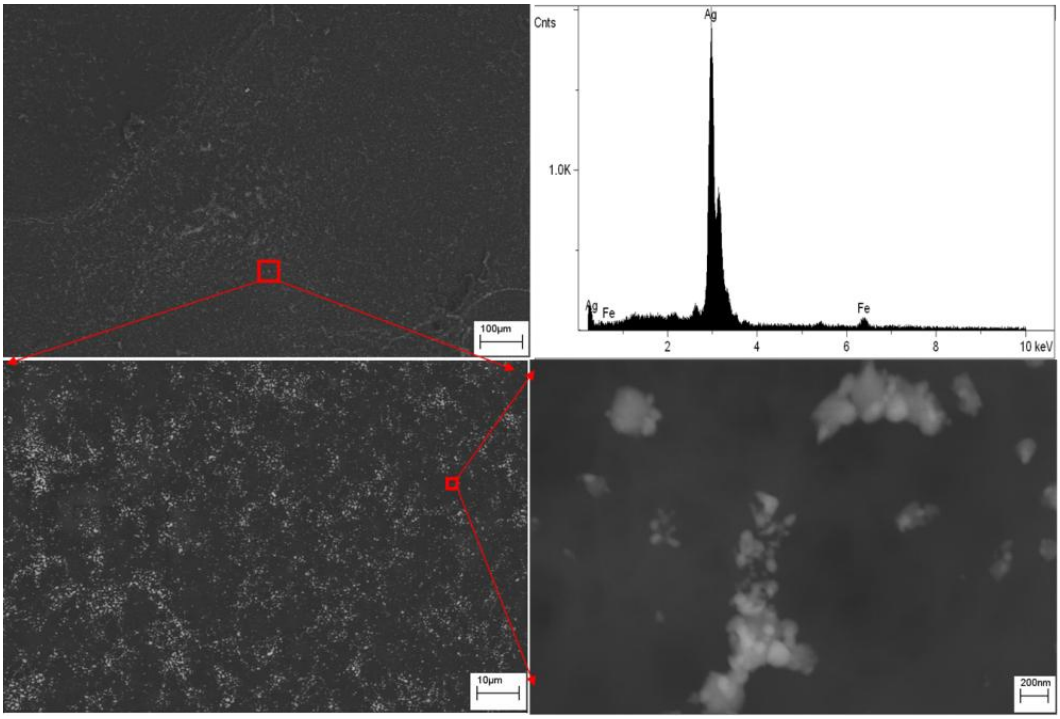

Figure 4.5: Scanning electron microscopic image of Ag deposited on 2 layers of chitosan at for 30 seconds at -0.5V at different magnification.

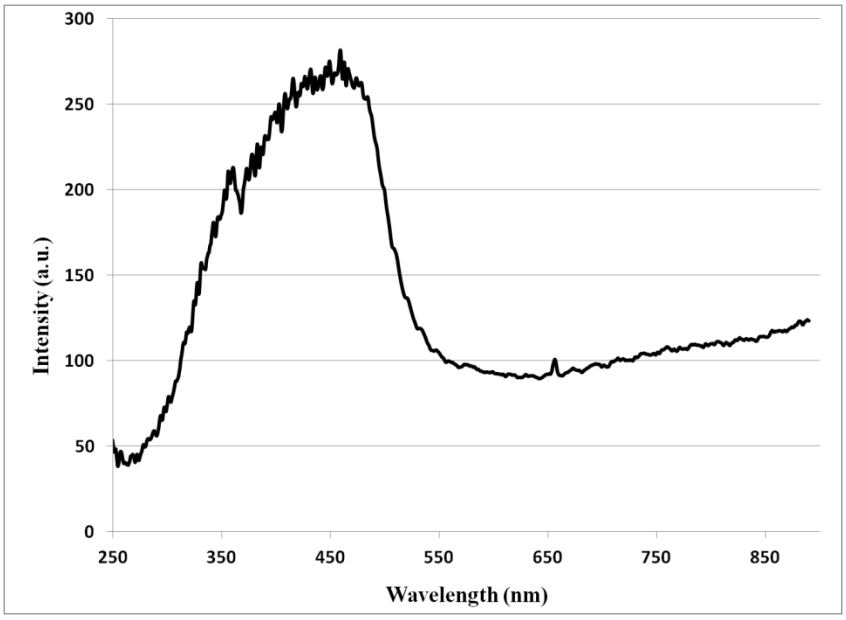

Figure 4.6: UV-Vis spectrum of Ag nanoparticles formed at -0.5V and 30 second deposition time.

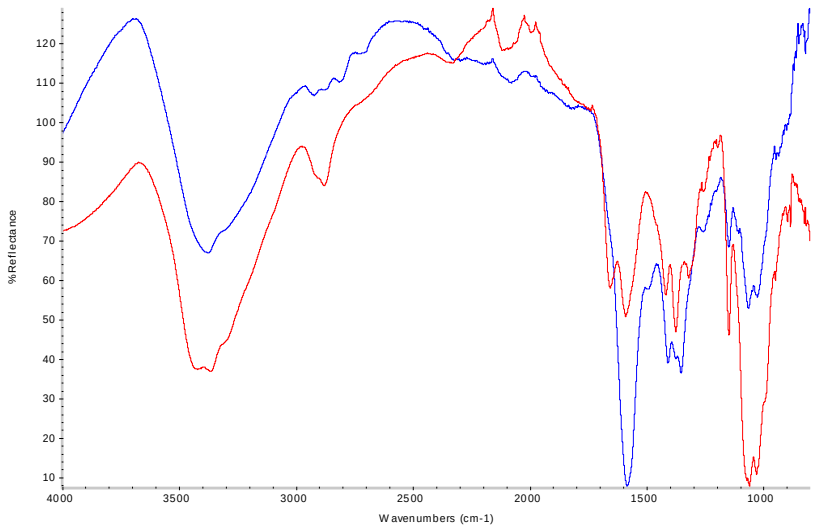

Figure 4.7: Synchrotron FTIR spectra from chitosan-Ag nanoparticles composite coating (blue) versus that from a pure chitosan coating (red).

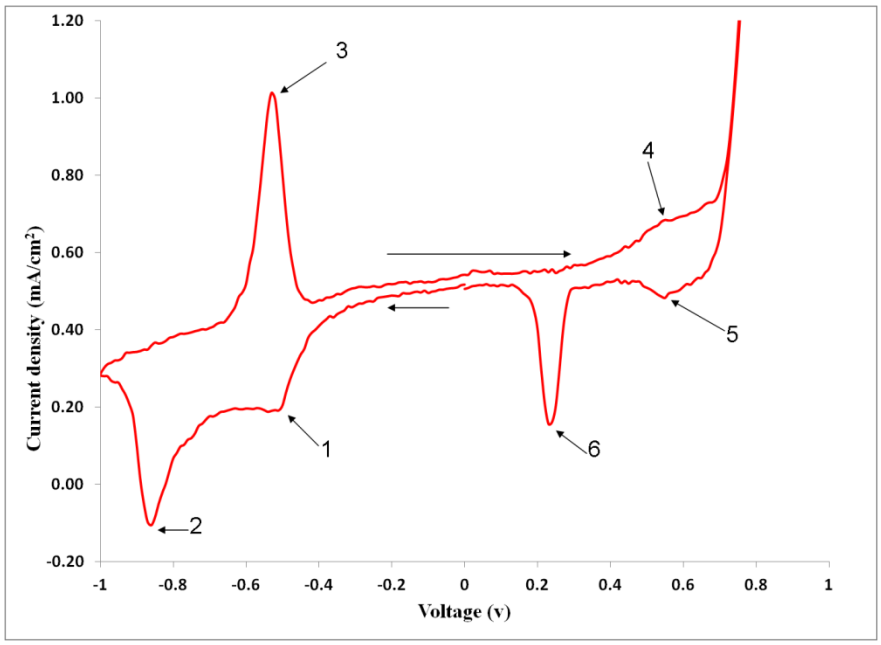

Figure 4.8: Cyclic voltammogram of oxygen reduction reaction using Ag nanoparticles as catalyst.

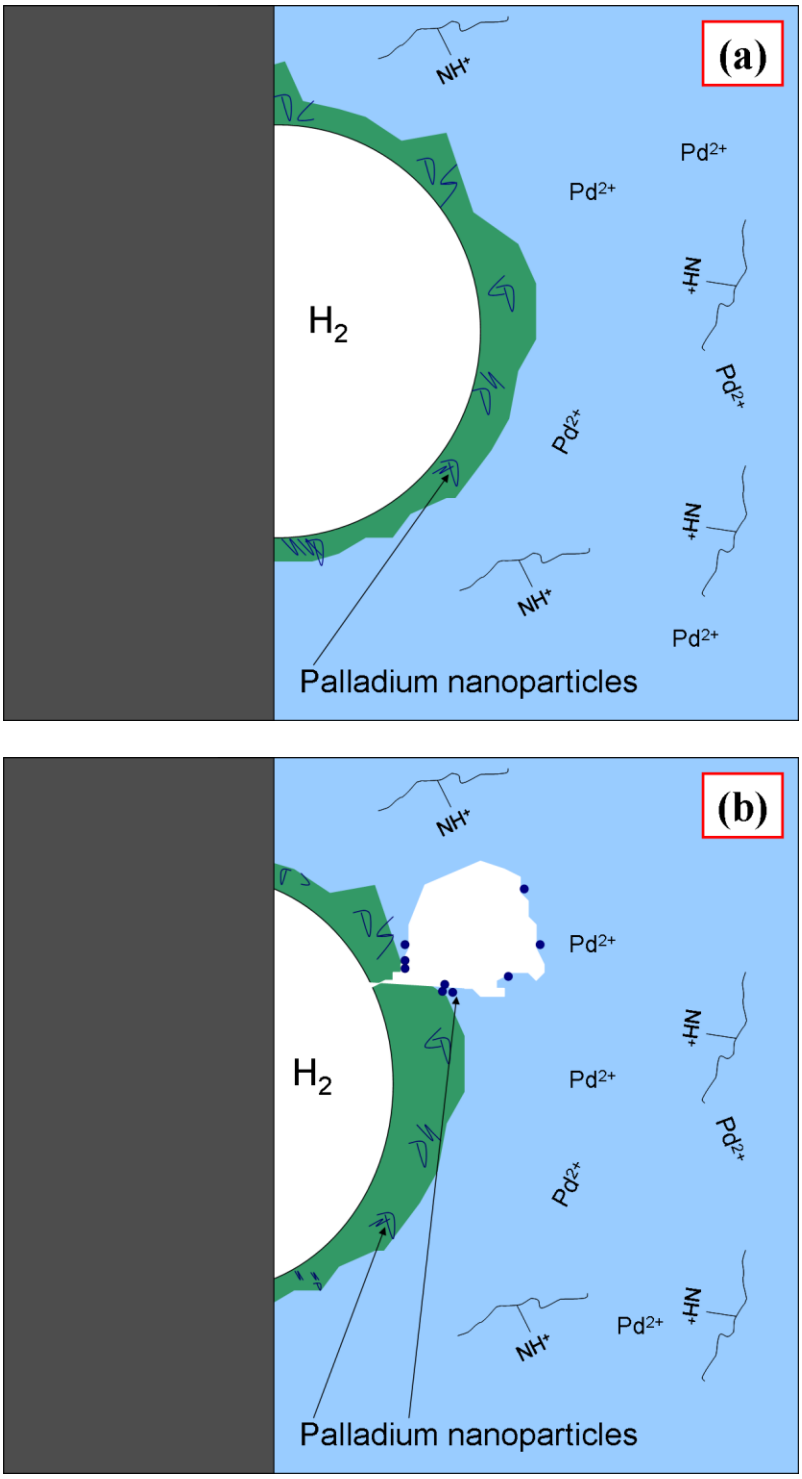

Figure 4.9: Schematic diagram of palladium nanoparticles formation.

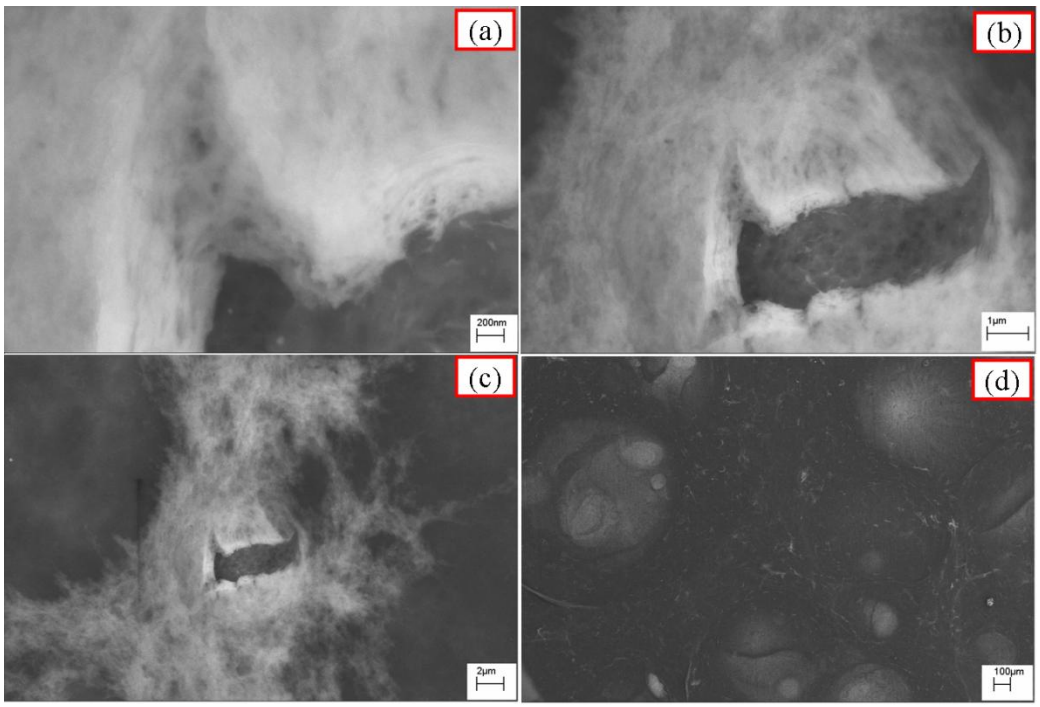

Figure 4.10: SEM image of palladium formed over hydrogen bubble.

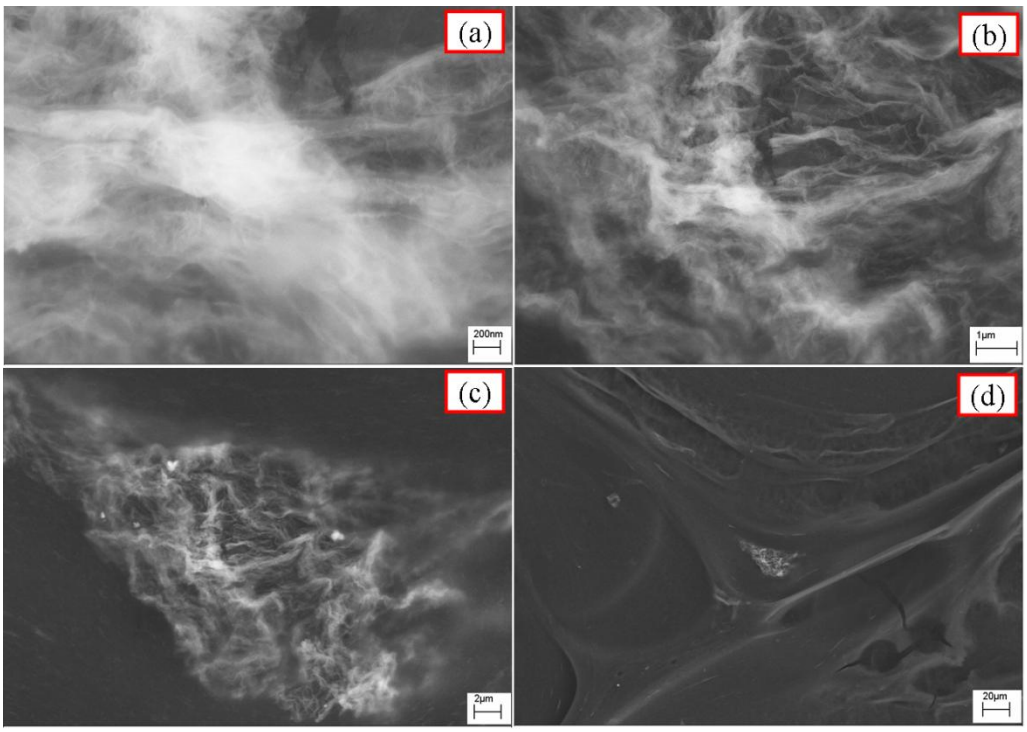

Figure 4.11: SEM image of palladium reduced by hydrogen.

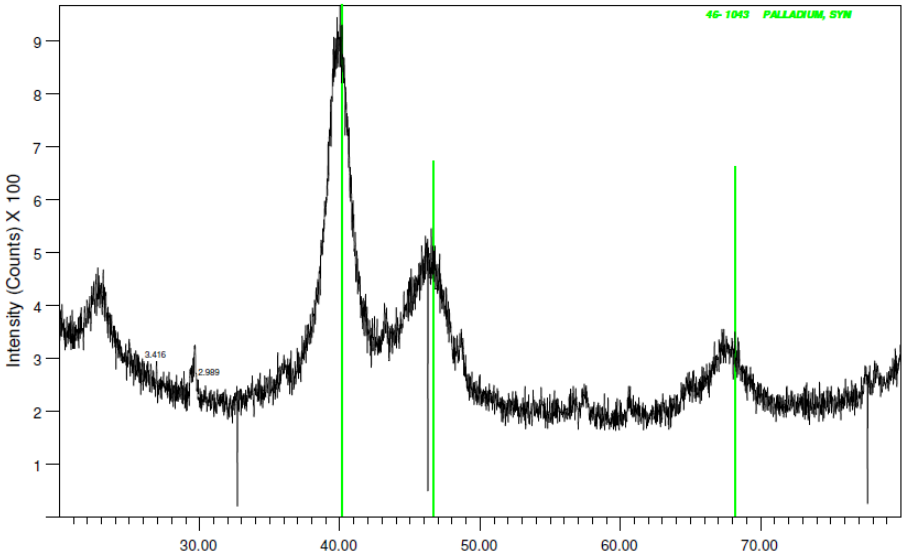

Figure 4.12: XRD pattern of deposited palladium.

Chapter 5 Future works.

Study of uranyl ion interaction with catechol showed that uranium can act as a catalyst in oxidative polycondensation of polyphenols. The results are significant for design of remediation process as well as for understanding humic formation.

1) In the next stage of these studies comparisons with polyphenols having hydroxyl group at different position of benzene ring should be done.

2) Effects of presence other functional group in ring should also be studied to estimate complexation with complex molecules like humic material.

3) Results from quantitative analysis into rate of reaction would be required for better understanding of the process.

4) Effects of salvation shell on polymerization need to be explored further.

The study of uranly interaction with oxalic acid showed strong bonding between uranly and carboxyl acid group leading to changes in solubility and thus transport properties uranium. The phenomenon is extremely useful in estimating behavior of uranium in natural environments due to acidic nature of humic material. To accurately predict association of uranium is natural organic matter further work must be done to access:

1) Change in complexation with change in acidic strength, with chain

length, number or carboxylic group and branching.

2) The effect of other functional group on nature of complex formed.

Electrochemical modification of polysaccharide was found to be a cheap, fast and environmentally friendly way to synthesize polymer derivatives at room temperature. Initial results are promising but the process needs further exploration before it can be commercialized, the works include:

1) A detailed study of physical and chemical properties of nitro-chitosan should be undertaken.

2) Study of change in chemistry with deposition made at different pHs should be undertaken. Initial results show that thickness of coating increases with pH, which can be explained in terms of zone of high pH. If the solution is already at pH5 a larger volume gets to pH>6.3 resulting in more deposition, but its effect on chemistry of hydrogel deposited is not known.

3) Metal binding and other properties of chloro-chitosan need to be investigated.

4) Attempts to create new derivatives of chitosan using other acids can be made.

5) Electrochemical modification of other water soluble polymers should be tried to find cheap alternative way of synthesizing derivatives.

6) Polymer emulsions can be explored for modification in mechanism

similar to formation of chloro-chitosan.

The deposited chitosan film on stainless steel formed a good base for subsequent deposition of silver nanoparticles. The size and distribution of nanoparticles was optimized for deposition voltage, time of deposition and layers of chitosan. The nanoparticles formed were found to be metallic and good catalyst for oxygen reduction reaction. The results show chitosan contributed towards stability of nanoparticles and the composite film can be a good candidate for electrode in alkaline fuel cells. To develop the composite film into electrode the works required will be:

1) Finding exact nature of bonding between chitosan and silver particles using NMR and EXAFS.

2) Finding the nature of conductivity through the chitosan film.

3) Exploring effects of cycling on nanoparticles and the film.

4) Finding effects of temperature on the composite.

5) Exploring poisoning effects due to presence of fuel or the byproducts.

6) Exploring aging effects on composite.

The synthesized composite should be tested for other expected application including photo catalysis and anti-bacterial applications. Attempts to reduce other catalytic metals should be made. One such attempt was made using palladium but it was found that palladium followed a completely different mechanism due to formation of $PdCl_4^{2-}$.

The particles were formed in this case by hydrogen reduction. This phenomenon opens a lot new opportunities by widening the electrochemical window beyond the potentials of electrolysis of water. Future work in this area should include:

1) Finding bonds between metal and chitosan

2) Testing conductivity for similarities and differences to silver deposition.

3) Testing catalytic activity of deposited metal.

4) Using chitosan solution without hydrochloric acid for palladium deposition.

References

1. Joan Ribas Gispert, *Coordination chemistry*, Wiley-VCH, 2008.

2. Ahmed H. Zewail, *The Chemical bond: structure and dynamics,* Academic Press, 1992.

3. Robert H. Grubbs, William Tumas, *Polymer Synthesis and OrganotransitionMetal Chemistry*. SCIENCE, VOL. 243, 915, 907-915, 1989

4. Derwent World Patents Index.

5. David E. Morse, Anna N. Glover, *MINERALS AND MATERIALS IN THE 20TH CENTURY—A REVIEW*, U.S. GEOLOGICAL SURVEY MINERALS YEARBOOK—2000.

6. C.N. Mulligan, R.N. Yong, B.F. Gibbs, *Remediation technologies for metal-contaminated soils and groundwater: an evaluation.* Engineering geology 2001, 60, 193-207.

7. S. P. Gubin, N. A. Kataeva, *Coordination Chemistry of Nanoparticles,* RUSSIAN JOURNAL OF COORDINATION CHEMISTRY, 2006, 32, 12, 849-857.

8. Stubbs JE, Elbert DC, Veblen DR, Zhu, C, *Electron microbeam investigation of uranium-contaminated soils from Oak Ridge, TN, USA*. Environmental Science & Technology. 2006, 40, 7, 2108-2113.

9. Abdelouas A, Lutze W, Nuttall E, *Chemical reactions of uranium in ground water at a mill tailings site. Journal of Contaminant Hydrology*. 1998, 34, 343–361.

10. Lottermoser BG, Ashley PM, *Tailings dam seepage at the rehabilitated Mary Kathleen uranium mine, Australia*. Journal of Geochemical Exploration. 2005, 85, 119– 137.

11. Brown P L,Guerin M, Hankin SI, Lowson RT, *Uranium and other contaminant migration in groundwater at a tropical Australian Uranium Mine*. Journal of Contaminant Hydrology. 1998,35,295–303

12. Winkelmann I, Thomas M, Vogl K, *Aerial measurements on uranium ore mining, milling and processing areas in Germany*. Journal of Environmental Radioactivity. 2001, 53 301-311.

13. Fernandes HM, Franklin MR, Veiga LHS, Freita P, Gomiero LA, *Management of uranium mill tailing: geochemical processes and radiological risk assessment*. J. Environ. Radioactivity. 1996, 30, I, 69-95.

14. Winde F, Jacobus WI, *The significance of groundwater-stream interactions and fluctuating stream chemistry on waterborne uranium contamination of streams - A case study from a gold mining site in South Africa*. Journal of Hydrology. 2004, 287, 178-196.

15. Papp Z, Dezso Z,Daroczy S, *Significant radioactive contamination of soil around a coal-fired thermal power plant*. Journal of Environmental Radioactivity.2002, 59,191-205.

16. Porcelli D, Swarzenski PW, *The Behavior of U- and Th- series Nuclides in groundwater*. In Uranium-series geochemistry Bourdon, B, Henderson, G.M, Lundstorm, C.C, Turner, S.P. Mineralogical Society of America: Washington, DC, 2003; Vol. 52, p 317-356.

17. Morris, DE, Allen, PG, Berg, JM , Chisholm - Brause CJ, Conradson SD, Donohoe RJ, Hess NJ, Musgrave J, Drew CT, *Speciation of uranium in Fernald soils by molecular spectroscopic methods: characterization of untreated soils*. Environ. Sci. Technol.1996, 30,2322-2331

18. Zhou P, Gu B, *Extraction of oxidized and reduced forms of uranium from contaminated soils: Effects of carbonate concentration and pH*. Environ. Sci. Technol.2005, 39,4435-4440.

19. Wood SA, *The role of humic substances in the transport and fixation of metals of economic interest (Au, Pt, Pd, U, V).* Ore Geology Reviews. 1996, 11, 1-31.

20. Stevenson F J, *Humus Chemistry: Genesis, composition, reactions*. Wiley New York, 1982.

21. Sanchez-Cortes S, Francioso O, Garcia-Ramos JV, Ciavatta C, Gessa C, *Catechol polymerization in the presence of silver surface.* Colloids and Surfaces A: Physicochemical and Engineering Aspects. 2001, 176, 177-184.

22. Dec J, Haider K, Bollag J, *Release of substituents from phenolic compounds during oxidative coupling reactions*. Chemosphere. 2003, 52, 549–556.

23. Aktas N, Tanyolac A: *Reaction conditions for laccase catalyzed polymerization of catechol*. Bioresource Technology. 2003, 87, 209-214.

24. Zeichmann W, *Die Darstellung von Huminsauren im heterogenen System mit neutraler Reaktion*. Z. Pflanzenernaehr. Dueng. Bodenkd. 1959, 84, 155−159.

25. Dubey S, Singh D, Misra RA, *Enzymatic synthesis and various properties of poly(catechol)*. Enzyme and Microbial Technology. 1998, 23,432-437.

26. Erhan, E, Keskinler B, Akay G, Algur, OF, *Removal of phenol from water by membrane-immobilized enzymes: Part I. Dead-end filtration*. Journal of membrane Science. 2002, 206, 361-373.

27. Colarieti ML, Toscano G, Greco JG, *Soil-catalyzed polymerization of phenolics in polluted waters*. Water Research. 2002 ,36, 3015-3022.

28. Colarieti ML, Toscano G, Ardi MR, Greco JG, *Abiotic oxidation of catechol by soil metal oxides*. Journal of Hazardous Materials B. 2006, 134, 161-168.

29. Zama K, Fukuoka A, Sasaki Y, Inagaki S, Fukushima Y, Ichikawa M, *Selective hydroxylation of benzene to phenol by photocatalysis of molybdenum complexes grafted on mesoporous FSM-16*. Catalysis Letters. 2000, 66, 4, 251-253.

30. Babcock WC, Friesen DT, Lachapelle ED, *Liquid membranes for separating uranium from vanadium and uranium from molybdenum*. Journal of Membrane Science. 1986, 26, 303-312.

31. Buck EC, Wronkiewicz DJ, Finn PA: Bates J.K, *New uranyl oxide hydrate phase derived from spent fuel alteration. Journal of Nuclear Materials*. 1997, 249,70-76.

32. Neunhauserer C, Berreck M, Insam H, *Remediation of soils contaminated with molybdenum using soil amendments and phytoremediation*. Water, Air, and Soil Pollution. 2001,128, 85–96.

33. Duarte RMBO, Santos EBH Duarte, Armando C, *Spectroscopic characteristics of ultrafiltration fractions of fulvic and humic acids isolated from an eucalyptus bleached Kraft pulp mill effluent*. Water Research. 2003,37, 4073–4080.

34. Miyasaka M, Yamazaki T, Tsuchida E, Nishide H, *Regioregular polythiophene with pendant phenoxyl radicals: a new high-spin organic polymer*. Macromolecules. 2000, 33, 8211-8217.

35. Shin YT, Shin SW, Shin J, Lee K, Cha M, *Pulsed laser deposition of a thin conjugated-polymer film*. Thin Solid Films. 2000, 360, 13-16.

36. Bruno FF, Nagarajan R, Stenhouse P, Yang K, Kumar J, Tripathy SK, Samuelson LA, *Polymerization of water-soluble conductive polyphenol using horseradish peroxidase*. J. MACROMOL. SCI.—PURE APPL. CHEM.; A. 2001,38,12, 1417–1426.

37. Zille A, Gornacka B, Rehorek A, Cavaco-Paulo A, *Degradation of azo dyes by Trametes villosa laccase over long periods of oxidative conditions*. Applied and environmental microbiology. 2005, 71, 11, 6711–6718.

38. Gorman-Lewis D, Fein JB, Burns PC, Szymanowski JES, Converse J, *Solubility measurements of the uranyl oxide hydrate phases metaschoepite, compreignacite, Na-compreignacite, becquerelite, and clarkeite*. Journal of Chemical Thermodynamics. 2008, 40, 980–990.

39. Fujii, T, Fujiwara K, Yamana H, Moriyama H, *Raman spectroscopic determination of formation constant of uranyl hydrolysis species* $(UO_2)_2(OH)_2^{2+}$. Journal of alloys and compounds. 2001,323-324, 859-863.

40. Maximovitch S, Barral G, Le Cras F, Claudet F, *Electrochemical incorporation of molybdenum in the passive layer of a 17% Cr ferritic stainless steel. Its influence on film stability in sulphuric acid and on pitting corrosion in chloride media.* Corrosion Science. 1995, 37, 2, 271-291.

41. Gulley-Stahl H, Hoganii PA, Schmidt WL, Wall SJ, Buhrlage A, Bullen HA, *Surface Complexation of Catechol to Metal Oxides: An ATR-FTIR,Adsorption, and Dissolution Study*. Environ. Sci. Technol. 2010, 44, 4116–4121.

42. Mazoyer P, Geantet C, Diehl F, Loridant S, Lacroix M, *Role of chelating agent on the oxidic state of hydrotreating catalysts*. Catalysis Today. 2008, 130, 75–79.

43. Arana J, Rendon ET, Rodriguez JMD, Melian JAH, Gonzalez O, Pena JP, *Highly concentrated phenolic wastewater treatment by the Photo-Fenton reaction, mechanism study by FTIR-ATR*. Chemosphere. 2001, 44, 1017-1023.

44. Borraccino R, Kharoune M, Giot R, Agathos SN, Nyns EJ; Naveay HP, Pauss A, *Abiotic transformation of catechol and 1-naphthol in aqueous solution-Influence of environmental factors*. Water Research. 2001, 35, 15, 3729-2737.

45. Horsman GP, Jirasek A, Vaillancourt FH, Barbosa CJ, Jarzecki AA, Xu C, Mekmouche Y, Spiro TG, Lipscomb JD, Blades MW, Turner RFB, Eltis LD, *Spectroscopic studies of the anaerobic enzyme-substrate complex of catechol 1,2-dioxygenase*. Journal of American Chemical Society. 2005, 127, 16882-16891.

46. Arana J, Fernandez RC, Gonzalez DO, Herrera MJA, Perez PJ, *Role of Cu in the Cu-TiO_2 photocatalytic degradation of dihydroxybenzenes*. Catalysis Today. 2005,101, 261–266.

47. Kubicki J, Halada G, Jha P, Phillips B, *Quantum Mechanical Calculation of Aqueous Uranium Complexes: Carbonate, Phosphate, Organic and Biomolecular Species.* Chem Cent J. 2009; 3: 10.; Published online 2009 August 18. doi: 10.1186/1752-153X-3-10.

48. Sever MJ, Wilker JJ, *Visible absorption spectra of metal–catecholate and metal–tironate complexes*. Dalton Trans. 2004, 1061 – 1072.

49. Wilkin RT, Su C, Ford RG, Paul CJ, *Chromium-removal process during groundwater remediation by a zerovalent iron permeable reactive barrier*. Environmental science and technology, 2005, 39, 4599-4605.

50. Wan Ngah WS, Kumari A, Fatinathan S, Ng PW, *Adsorption of chromium from aqueous solution using chitosan beads.* Adsorption 2006, 12:249-257.

51. Baroni P, Vieira RS, Meneghetti E, da Silva MGC, Beppu MM, *Evaluation of batch adsorption of chromium ions on natural and*

crosslinked chitosan membranes. Journal of Hazardous Materials 2008, 152, 1155-1163.

52. Loyaux-lawniczak S, Lecomte P, *Chromium in a polluted groundwater: Redox process and immobilization in soils.* Environmental science and technology, 2001, 35, 1350-1357.

53. Wang J, Peng R,Bao Z, Yang J, Chen S, Liu Q, *Quick removal of chromium (VI) ions from aqueous solution by chitosan and ferrous ions.* IEEE 4th International conference on Bioinformatics and Biomedical Engineering, 2010, 1-4.

54. Bailey SE, Olin TJ, Bricka RM, Adrian DD, *A review of potentially low-cost sorbents for heavy metals*, Water Research, 1999, 33, 11, 2469-2479.

55. Modrzejewska Z, Maniukiewicz W, Wojtasz-pajak A, *Determination of Hydrogel chitosan membrane structure*, Polish Chitin society, monograph XI, 2006, 113-121.

56. Nunthanid J, Puttipipatkhanachorn S, Yamamoto K, Peck GE, *Physical properties and molecular behavior of chitosan films.* Drug development and industrial pharmacy, 2001, 27(2), 143-157.

57. Guibal E, *Interactions of metal ions with chitosan-based sorbents: a review.* Separation and Purification Technology, 2004, 38, 43-74.

58. Rojas G, Silva J, Flores JA, Rodriguez A, Ly M, Maldonado H, *Adsorption of chromium onto cross-linked chitosan.* Separation and purification technology 2005, 44, 31-36.

59. Mourya VK, Inamdar NN, *Chitosan-modifications and applications: Opportunities galore.* Reactive and Functional Polymers, 2008, 68, 1013-1051.

60. Halada GP, Jha P, Nelson K, Zhao W, Korach CS, Neiman A, Lee SJ, *Formation and Characterization of Chitosan-Based Coatings on Stainless Steel*. Biomaterials, ACS symposium series, 2010, 8, 159-171.

61. Sun X, Peng B, Ji Y,Chen J, Li D, *Chitosan(chitin)/cellulose composite biosorbents prepared using ionic liquid for heavy metal ions adsorption*. American institute of chemical Engineers. 2009 55,8, 2062-2069.

62. Fernendes R, Wu LQ, Chen T, Yi H, Rubloff GW, Ghodssi R, Bentley WE, Payne GF, *Electrochemically Induced Deposition of a Polysaccharide Hydrogel onto a Patterned Surface*. Langmuir 2003, 19, 4058-4062.

63. Beard B, *Cellulose nitrate as a binding energy reference in N(1s) XPS studies of nitrogen-containing organic molecules*, Applied Surface Science, 1990, 45, 3, 221-227.

64. Berger P, Vel Leitner NK, Dore M, Legube B, *Ozone and hydroxyl radicals induced oxidation of glycine*, Water Research 1999, 33, 2, 433-441.

65. Gad YH, *Preparation and characterization of poly(2-acrylamido-2-methypropane sulfonic acid)/chitosan hydrogel using gamma irradiation and its application in wastewater treatment*. Radiation Physics and Chemistry. 2008, 77, 1101-1107.

66. Hena S, *Removal of chromium hexavalent ion from aqueous solutions using biopolymer chitosan coated with poly 3-methyl thiophene polymer*., Journal of hazardous Materials. 2010, 181, 474-479

67. Verma BM, Krishnaiah A, Talbott JL, Edgar SD, *Removal of Hexavalent Chromium from wastewater using a new composite chitosan biosorbent. Environmental Science and Technology*. 2003, 37, 4449-4456

68. Aydin YA, Aksoy ND, *Adsorption of chromium on Chitosan: Optimization, kinetics and thermodynamics*. Chemical Engineering Journal 2009, 151, 188-194.

69. Aksu Z, Gonen F, Demircan Z, *Biosorption of chromium(VI) ions by Mowital B3OH resin immobilized activated sludge in a packed bed: comparison with granular activated carbon. Process. Biochem.* 2002, 38, 175-186.

70. Baran A, Bicak E, Baysal SH, Onal S, *Comparative studies on the adsorption of Cr(VI) ions on to various sorbents*. Bioresource technology 2006, 98, 661-665

71. Sabharwal S, Ramnani SP, *Adsorption behavior of Cr(VI) onto radiation crosslinked chitosan and its possible application for the*

treatment of wastewater containing Cr(VI). Reactive & Functional Polymers 2006, 66, 902–909

72. Xin-jiang H, Wang JS, Liu YG, Li X, Zeng G, Bao Z, Zeng X, Chen A, Long F. *Adsorption of chromium (VI) by ethylenediamine-modified cross-linked magnetic chitosan resin: Isotherms, Kinetics and thermodynamics*. Journal of Hazardous Materials. 2011, 185, 306-314.

73. Gabriele C, Perathoner S, *Catalysis and sustainable (green) chemistry.* Catalysis Today 2003, 77, 287–297.

74. Ohgi Y, Ishihara A, Matsuzawa K, Mitsushima S, Ota K, *Catalytic activity of zirconium based cathode without platinum for oxygen reduction reaction*, ECS Transactions, 2010, 33 (1), 609-624.

75. Anastas PT, Kirchhoff MM, Williamson TC, *Catalysis as a foundational pillar of green chemistry*, Applied Catalysis A: General, 2001, 221, 3–13.

76. Jan JS, Chen PJ, Ho YH, *Bioassisted synthesis of catalytic gold/silica nanotubes using layer-by-layer assembled polypeptide templates*, Journal of Colloid and Interface Science. 2011, 358 409–415.

77. McLean GF, Niet T, Prince-Richard S, Djilali N, *An assessment of alkaline fuel cell technology*. International Journal of Hydrogen Energy. 2002, 27, 507 – 526.

78. Catalysis for Energy: Fundamental Science and Long-Term Impacts of the U.S. Department of Energy Basic Energy Science Catalysis Science Program, Board on Chemical Sciences and Technology, National Academies press (2009)

79. Adlim M, Bakar MA, Liew KY, Ismail J, *Synthesis of chitosan-stabilized platinum and palladium nanoparticles and their hydrogenation activity*. Journal of Molecular catalysis A: Chemical, 2004, 212, 141-149.

80. Astruc D, Nanoparticles and Catalysis, Wiley-VCH, 2008, isbn 978-3-527-31572-7

81. Gustav KH, Wiberg K, Mayrhofer JJ, Arenz M, *Investigation of the Oxygen Reduction Activity of non-Platinum Catalysts – a RDE Methodology*, ECS Transactions, 2009, 19 (31), 37-46.

82. Yizhong L, Chen W, *Size effect of silver nanoclusters on their catalytic activity for oxygen electro-reduction*, Journal of Power Sources. 2012, 197, 107– 110.

83. Peng Z, Wu J, Yang H, *Synthesis and Oxygen Reduction Electrocatalytic Property of Platinum Hollow and Platinum-on-Silver Nanoparticles*. Chem. Mater. 2010, 22, 1098–1106

84. Lee CL, Wu WC, Wu CC, Chiou HP, Chao YJ, *Electrostatic Preparation of Graphite Nanofiber-Supported Ag Nanoparticles*. Journal of The Electrochemical Society. 2010, 157, 11, K232-K235

85. Lee CL, Chiou HP, Syu CM, Liu CR, Yang CC, Syu CC, *Displacement triangular Ag/Pd nanoplate as methanol-tolerant electrocatalyst in oxygen reduction reaction*. International journal of hydrogen energy. 2011, 36, 12706 -12714

86. Lee CL, Chiou HP, Chang KC, Huang CH, *Carbon nanotubes-supported colloidal Ag-Pd nanoparticles as electrocatalysts toward oxygen reduction reaction in alkaline electrolyte*. International journal of hydrogen energy 2011, 36, 2759-2764

87. Martínez-Casillas DC, Solorza-Feriaa O, *Synthesis and Characterization of Bimetallic PdM Nanoparticles (M =Ag, Cu) Oxygen Reduction Electrocatalysts*, ECS Transactions, 2009, 20 (1), 275-280.

88. Jiang L, Hsu A, Chu D, Chen R, *A highly active Pd coated Ag electrocatalyst for oxygen reduction reactions in alkaline media.* Electrochimica Acta. 2010, 55, 4506–4511

89. Guo J, Li H, He H, Chu D, Chen R, *CoPc- and CoPcF16-Modified Ag Nanoparticles as Novel Catalysts with Tunable Oxygen Reduction Activity in Alkaline Media*, J. Phys. Chem. 2011, 115, 8494–8502

90. Lima FHB, deCastro JFR, Ticianelli EA, *Silver-cobalt bimetallic particles for oxygen reduction in alkaline media*. Journal of Power Sources 2006, 161, 806–812.

91. Dahms H, Croll IM, *The anomalous codeposition of nickel-iron alloys*. J. Electrochem Soc., 1965, 112, 771-775.

92. Bhui DK, Bar H, Sarkar P, Sahoo GP, De SP, Misra A, *Synthesis and UV–vis spectroscopic study of silver nanoparticles in aqueous SDS solution.* Journal of Molecular Liquids 2009, 145, 33–37.

93. Meng XK, Tang SC, Vongehr S, *A Review on Diverse Silver Nanostructures.* J. Mater. Sci. Technol., 2010, 26(6), 487–522.

94. Saraidarov T, Levchenko V, Popov I, Reisfeld R, *Shape control synthesis of spheroid and rod-like silver nanostructures in organicinorganic sol-gel composite.* Superlattices and Microstructures 2009,46, 171-175.

95. Guo J, Hsu A, Chu D, Chen R, *Improving Oxygen Reduction Reaction Activities on Carbon-Supported Ag Nanoparticles in Alkaline Solutions.* J. Phys. Chem. 2010, 114, 4324–4330.

96. Miah MR, Ohsaka T, *Observation of 'inverted peak' during molecular oxygen reduction at Au electrode in alkaline media*. Electrochimica Acta. 2007, 52, 6378–6385.

97. Morrison MM, Roberts JL, Sawyer DT, *Oxidation-Reduction Chemistry of Hydrogen Peroxide in Aprotic and Aqueous Solutions.* Inorganic Chemistry, 1979, 18, 7,1971-1973.